An Analytic Description of the Structure and Evolution of Growing Deep Cumulus Updrafts

HUGH MORRISON

National Center for Atmospheric Research,[a] *Boulder, Colorado*

(Manuscript received 9 August 2016, in final form 16 November 2016)

ABSTRACT

New theoretical analytic expressions are derived for the evolution of a passive scalar, buoyancy, and vertical velocity in growing, entraining moist deep convective updrafts. These expressions are a function of updraft radius, height, convective available potential energy (CAPE), and environmental relative humidity R_H. They are quantitatively consistent with idealized three-dimensional moist updraft simulations with varying updraft sizes and in environments with differing R_H. In particular, the analytic expressions capture the rapid decrease of buoyancy with height due to entrainment for narrow updrafts in a dry environment despite large CAPE. In contrast to the standard entraining-plume model, the theoretical expressions also describe the effects of engulfment of environmental air between the level of free convection (LFC) and height of maximum buoyancy (HMB) required by mass continuity to balance upward acceleration of updraft air (i.e., dynamic entrainment). This organized inflow sharpens horizontal gradients, thereby enhancing smaller-scale lateral turbulent mixing below the HMB. For narrow updrafts in a dry environment, this enhanced mixing leads to a negatively buoyant region between the LFC and HMB, effectively cutting off the region of positive buoyancy at the HMB from below so that the updraft structure resembles a rising thermal rather than a plume. Thus, it is proposed that a transition from plume-like to thermal-like structure is driven by dynamic entrainment and depends on updraft width (relative to height) and environmental R_H. These results help to bridge the entraining-plume and rising-thermal conceptual models of moist convection.

1. Introduction

It has long been established that entrainment of environmental air plays a critical role in the evolution of observed moist convection. Early ideas about entrainment in cumulus clouds were based on various conceptual models of convection driven by a point source of buoyancy (e.g., see Turner 1973): 1) a steady-state entraining plume associated with a steady buoyancy source (Morton et al. 1956); 2) a rising, entraining thermal associated with a pulse of buoyancy (Batchelor 1954; Morton et al. 1956); and 3) a starting plume representing a growing plume with a buoyancy source that is switched on and held fixed (Turner 1962). The behavior of the upward-moving fluid in these models differs considerably. Entraining plumes have an increase in width of the buoyant fluid in the plume with height through the process of entraining environmental fluid, with a decrease of the buoyancy within the plume above its source from dilution. Thermals have the structure of an isolated, entraining bubble of buoyant fluid rising through the surrounding environmental fluid, with nonbuoyant environmental fluid below the thermal in its wake. Thus, in contrast to plumes the buoyant fluid is "cut off" from its original buoyancy source. Starting plumes have characteristics of both plumes and thermals; well behind the head of the rising plume the motion is like that of a steady-state plume, while at the head it behaves more like a thermal.

Conservation equations for mass, momentum, and thermal energy of steady-state plumes can be derived from dimensional analysis (see Emanuel 1994). For the mass flux, this gives $d(R^2M)/dz = 2R\mu M$ (Emanuel 1994), where M is the mass flux, z is height, R is plume radius, and μ is a proportionality constant related to fractional entrainment. This can be simplified for a plume of constant R to give

$$\frac{1}{M}\frac{dM}{dz} = \varepsilon = \frac{2\mu}{R}, \tag{1}$$

[a] The National Center for Atmospheric Research is sponsored by the National Science Foundation.

Corresponding author e-mail: Hugh Morrison, morrison@ucar.edu

DOI: 10.1175/JAS-D-16-0234.1

where ε is a fractional entrainment rate and $\mu \approx 0.09$ from laboratory tank experiments of plumes (Morton et al. 1956). The structure and behavior of rising thermals differs considerably from steady-state plumes. This manifests as differences in the vertical perturbation pressure gradient force, usually considered as a drag force for thermals and as a virtual mass coefficient with an effective inertia for plumes, as well as differences in entrainment and mixing. For the latter, a set of conservation equations can also be derived from dimensional analysis for rising thermals similar to (1), but with different (generally larger) entrainment rates compared to plumes (Morton et al. 1956; Emanuel 1994). Squires and Turner (1962) presumed that a realistic model of cumulus convection should include features of both the plume and thermal conceptual models. While questions remain as to which model provides the best description of real moist convection, most contemporary convection parameterizations have features more in line with plumes than thermals (de Rooy et al. 2013).

Over the past several decades many studies have called into question the realism of representing moist updrafts in convection schemes using the standard entraining-plume model [e.g., see the review of de Rooy et al. (2013)]. These criticisms have often centered on the heterogeneous structure of real cloudy updrafts, in contrast to the horizontally homogeneous updraft properties typically assumed in plume-based schemes. For example, (1) does not directly address the role of detrainment near cloud edge that can occur from mixing of environmental air and cloudy updraft air. Based on aircraft observations, studies have shown that updraft air is often strongly diluted from mixing with the environment, but cloud height is more consistent with the growth of less-dilute parcels (e.g., Warner 1970; Warner 1977; Jonas 1990). An explanation for this behavior was proposed by Raymond and Blyth (1986) based on "buoyancy sorting," whereby upon mixing of entrained environmental air with some portion of updraft air, if the resulting mixture is positively buoyant it remains within the updraft and continues to rise, and if it is negatively buoyant it is detrained and descends to its level of neutral buoyancy. Buoyancy sorting has served as the conceptual basis for several schemes (e.g., Kain and Fritsch 1990; Emanuel 1991; Bretherton et al. 2004). Other inconsistencies between the standard plume model and cloud-resolving model simulations have also been emphasized, such as the stochastic nature of entrainment as growing updrafts undergo Poisson-process entrainment events (Romps and Kuang 2010; Romps 2016).

Upward acceleration of buoyant updraft air implies horizontal entrainment of environmental air, explicitly linking entrainment to the vertical acceleration of air within updrafts by mass continuity. This type of entrainment associated with organized convective-scale flow has been referred to as "dynamic entrainment," distinguished from entrainment driven by smaller-scale turbulent mixing ("turbulent entrainment") (e.g., Houghton and Cramer 1951; Asai and Kasahara 1967; Tiedtke 1989; Bechtold et al. 2008; de Rooy and Siebesma 2010). A similar mechanism occurs with the vertical deceleration of air in updrafts, leading to dynamic detrainment (de Rooy et al. 2013). The plume model in (1) can be modified to account for dynamic entrainment, expressed as (e.g., de Rooy and Siebesma 2010)

$$\frac{1}{M}\frac{dM}{dz} = \varepsilon_{\text{turb}} + \varepsilon_{\text{dyn}}, \tag{2}$$

where $\varepsilon_{\text{turb}}$ and ε_{dyn} are fractional turbulent and dynamic entrainment rates, respectively. Fractional detrainment associated with dynamic and/or turbulent detrainment is also often included in such expressions but is excluded in (2) for the sake of discussion since the focus here is on entrainment. Numerous parameterizations have been proposed for $\varepsilon_{\text{turb}}$ and ε_{dyn} as functions of saturation specific humidity, relative humidity, moisture convergence, or momentum convergence, to name a few [see de Rooy et al. (2013) for an overview].

Large-eddy simulation (LES) has been instrumental for understanding entrainment and improving its representation in convection schemes. Several studies have used LES to assess and improve entrainment rate formulations (e.g., Siebesma and Cuijpers 1995; Neggers et al. 2002; Kuang and Bretherton 2006; de Rooy and Siebesma 2010). Typically, ε has been estimated from LES following the variation of conserved variables with height, assuming updrafts can be represented by steady-state entraining plumes (e.g., Siebesma and Cuijpers 1995; Siebesma et al. 2003; de Rooy et al. 2013). On the other hand, direct calculation of entrainment rates using passive tracers in LES has shown that the standard entraining-plume assumption can substantially underestimate ε, by approximately a factor of 2 (Romps 2010; Dawe and Austin 2011a). Romps (2010) described this inconsistency as arising from differences in tracer amounts in the near and far updraft environments that cannot be accounted for by the standard plume approach.

This paper also critiques the entraining-plume model, but from a theoretical perspective. Herein, analytic expressions for the evolution of a passive scalar, buoyancy, and vertical velocity are derived as a simple analog for growing moist convective updrafts. These expressions are

compared to three-dimensional numerical simulations, with individual updrafts initiated by adding warm bubbles near the level of free convection (LFC). The purpose is to develop simple scaling relationships that provide a straightforward physical interpretation of key factors affecting moist deep convection, intended to augment detailed LES studies. This study also bridges aspects of the plume and thermal conceptual models of moist convection; it is argued that a key linkage between these models is dynamic entrainment, and specifically its relationship to the organized updraft structure (the vertical distribution of buoyancy in particular) and its role in driving smaller-scale turbulent mixing.

The remainder of the paper is organized as follows. Section 2 provides a derivation of the theoretical expressions. The numerical simulations are described in section 3 and compared with the analytic expressions in section 4. Section 5 summarizes key results and provides conclusions.

2. Derivation of theoretical expressions

In this section, analytic expressions are derived for the evolution of a passive scalar $C_{\rm Tr}$, buoyancy B, and vertical velocity w in a simple model of growing moist convection. The initial focus is on $C_{\rm Tr}$ because the derivation is straightforward—in essence, equations for the transport of a passive scalar are the same as those for dry convective updrafts. More complicated expressions for the evolution of B and w are then derived after. These expressions give $C_{\rm Tr}$, B, and w at the updraft center, which simplifies the derivation since horizontal advection is zero at the center by symmetry in the axisymmetric framework employed here. However, it is emphasized that horizontal advection associated with inflow of environmental air into the updraft (dynamic entrainment) is indirectly important at the updraft center because it modifies horizontal gradients and hence smaller-scale lateral turbulent mixing, as will be shown in section 2d.

Idealized numerical simulations from Morrison (2016a, see Fig. 1 therein) indicate net horizontal convergence across updrafts from the LFC to just below the height of maximum buoyancy (HMB), nearly zero convergence at the HMB itself, and net divergence above. This structure is primarily explained by the field of buoyant perturbation pressure p_B and the associated horizontal perturbation pressure gradient force: $p_B > 0$ approximately above the HMB, relative to the environment (meaning a horizontal perturbation pressure gradient force directed outward from the updraft), with $p_B < 0$ below (meaning an inward-directed horizontal perturbation pressure gradients force). This structure is dictated by the dependence of p_B on vertical gradients of buoyancy; for a vertically symmetric updraft buoyancy profile—that is, buoyancy that is a mirror image above and below the HMB—single normal Fourier–Bessel mode solutions show that p_B is exactly antisymmetric around the HMB. This links regions of net horizontal convergence and divergence directly to the vertical distribution of updraft buoyancy, keeping in mind that dynamic perturbation pressure must be included for the pressure field to be consistent with mass continuity. As updrafts grow the HMB rises over time, and hence so do the regions of net convergence and divergence.

Since net convergence near the HMB is close to zero, the effects of dynamic entrainment at this level are small. On the other hand, net horizontal convergence from the LFC to just below the HMB drives dynamic entrainment, with important effects on updraft properties there. This picture notably differs from previous studies that have included dynamic entrainment within a plume-like framework (e.g., Asai and Kashara 1967; de Rooy and Siebesma 2010). This is because these studies applied dynamic entrainment at all levels where the mass flux increases with height, inconsistent with near-zero convergence at the HMB and net divergence above. Reflecting this distinction, the expressions herein are first derived at the HMB assuming dynamic entrainment has a negligible impact at this level. Expressions valid between the LFC and HMB at the updraft center are then derived by including the effects of dynamic entrainment.

a. Passive scalar

We first consider the evolution of $C_{\rm Tr}$ at the HMB as it rises. Performing a Reynolds averaging of the scalar conservation equation in axisymmetric cylindrical coordinates gives

$$\frac{\partial \overline{C}_{\rm Tr}}{\partial t} = -\overline{u}\frac{\partial \overline{C}_{\rm Tr}}{\partial r} - \overline{w}\frac{\partial \overline{C}_{\rm Tr}}{\partial z} - \frac{1}{r}\frac{\partial (r\overline{u'C'_{\rm Tr}})}{\partial r} - \frac{\partial (\overline{w'C'_{\rm Tr}})}{\partial z}, \tag{3}$$

where u and w are the radial and vertical winds, r is radial distance from the updraft center, z is height, t is time, unprimed quantities represent the organized updraft-scale flow, and primes denote fluctuations from this organized flow. For ease of interpretation, the organized-flow quantities are written in advective form, while the fluctuating quantities are written in flux form, assuming constant air density. Hereafter the overbars

denoting Reynolds-averaged quantities are omitted except for the turbulent flux terms. The vertical turbulent flux divergence is neglected for simplicity, which assumes that lateral turbulent mixing dominates.[1]

By axisymmetry horizontal gradients must vanish at $r = 0$ in the presence of mixing, implying that $\overline{u'C'_{\mathrm{Tr}}} = 0$ at $r = 0$. On the other hand, nonzero gradients imply $\overline{u'C'_{\mathrm{Tr}}} \neq 0$ away from the updraft center and hence a nonzero horizontal flux divergence across the updraft. The local flux divergence is approximated by its horizontally averaged value from $r = 0$ to $r = L$:

$$\frac{1}{r}\frac{\partial(r\overline{u'C'_{\mathrm{Tr}}})}{\partial r} \approx \frac{1}{\pi L^2}\int_0^{2\pi}\int_0^{L}\frac{1}{r}\frac{\partial(r\overline{u'C'_{\mathrm{Tr}}})}{\partial r} r\,dr\,d\theta = \frac{2}{L}\overline{u'C'_{\mathrm{Tr}}}\Big|_{r=0}^{r=L} = \frac{2}{L}(\overline{u'C'_{\mathrm{Tr}}})_L, \tag{4}$$

where L is a turbulent mixing length. The value of $\overline{u'C'_{\mathrm{Tr}}}$ at $r = L$, $(\overline{u'C'_{\mathrm{Tr}}})_L$, is estimated by applying an eddy diffusion approach (Kuo 1962; Asai and Kasahara 1967; de Rooy and Siebesma 2010):

$$(\overline{u'C'_{\mathrm{Tr}}})_L = -K_C\frac{\partial C_{\mathrm{Tr}}}{\partial r}, \tag{5}$$

where K_c is an exchange coefficient approximated as

$$K_C = \frac{k^2L^2}{P_r}\left|\frac{\partial w}{\partial r}\right|. \tag{6}$$

Here k is a constant and $P_r \approx 1/3$ is a turbulent Prandtl number (Deardorff 1972) also applied in the subgrid-scale mixing scheme for the numerical simulations in section 3.

Combining (3)–(6) gives

$$\frac{\partial C_{\mathrm{Tr}}}{\partial t} = -u\frac{\partial C_{\mathrm{Tr}}}{\partial r} - w\frac{\partial C_{\mathrm{Tr}}}{\partial z} + \frac{2k^2L}{P_r}\frac{\partial C_{\mathrm{Tr}}}{\partial r}\left|\frac{\partial w}{\partial r}\right|. \tag{7}$$

Assuming $\partial w/\partial r \sim -w/R$ and $\partial C_{\mathrm{Tr}}/\partial r \sim -(C_{\mathrm{Tr}} - C_{\mathrm{Tr},E})/R$, where w and C_{Tr} are values at the updraft center and $C_{\mathrm{Tr},E}$ is the scalar value in the environment (it is assumed $w = 0$ in the environment), taking (7) as a material derivative following the updraft flow—that is, $d/dt = \partial/\partial t + u\partial/\partial r + w\partial/\partial z$ and using the chain rule such that $d/dt = (d/dz)(dz/dt) = (d/dz)w$—(7) is expressed as

$$w\frac{dC_{\mathrm{Tr}}}{dz} - \frac{2k^2Lw(C_{\mathrm{Tr}} - C_{\mathrm{Tr},E})}{P_rR^2} = 0. \tag{8}$$

In this quasi-Lagrangian framework, the material derivative is taken to follow the HMB, which closely tracks the growth of the cloud/updraft top until the dissipation stage in the numerical simulations presented in section 3. Note that interpreting the increase in height of the HMB as it rises over time as a material derivative is an approximation since it does not strictly follow air parcel trajectories; analysis of the simulations shows that the upward movement of the HMB is about a factor of 1.5–2 smaller than w at this level.

Dividing (8) by w, its form is similar to the expression for scalar transport in the steady-state entraining-plume model of Betts (1975) and subsequent studies:

$$\frac{dC_{\mathrm{Tr}}}{dz} = -\varepsilon_C(C_{\mathrm{Tr}} - C_{\mathrm{Tr},E}), \tag{9}$$

where ε_C is a fractional scalar entrainment rate. An expression for C_{Tr} at height z, $C_{\mathrm{Tr},z}$, is derived by dividing (8) by w and analytically integrating (without approximation) from the LFC to height z (i.e., where z is understood to be the height of the HMB as it increases over time), assuming constant R, to give

$$C_{\mathrm{Tr},z} = C_{\mathrm{Tr},0}e^{-2k^2Lz/(P_rR^2)}, \tag{10}$$

where $C_{\mathrm{Tr},0}$ is the value of C_{Tr} at the LFC and $C_{\mathrm{Tr},E} = 0$ for simplicity and consistency with the simulations discussed in section 3. An alternative solution is derived by dividing (8) by w, using a linear estimate of the average value of $C_{\mathrm{Tr}} \sim (C_{\mathrm{Tr},z} - C_{\mathrm{Tr},0})/2$ on the right-hand side, and integrating the resulting expression from the LFC to z:

$$C_{\mathrm{Tr},z} = \frac{1 - k^2Lz/(P_rR^2)}{1 + k^2Lz/(P_rR^2)}C_{\mathrm{Tr},0}. \tag{11}$$

Differences in $C_{\mathrm{Tr},z}$ using (10) and (11) are less than a few percent for the tests described in section 4, which is not surprising since the form of (11) is an approximation of the infinite power series expression for e^{-x} valid when $x \ll 2$; that is, $e^{-x} \approx (1 - x/2)/(1 + x/2)$. Hereafter we focus on (11) since a similar approximation is used to derive analytic equations for B and w in sections 2b and 2c. Note that if R is constant in time, then (10) and (11)

[1] A debate on the role of lateral versus cloud-top mixing has been ongoing for several decades. Observational evidence for cloud-top entrainment comes from mixing diagrams of conserved variables (e.g., Paluch 1979; "Paluch" diagrams). On the other hand, there has been criticism of this interpretation of the data (Taylor and Baker 1991; Siebesma 1998; de Rooy et al. 2013; Boing et al. 2014) since "buoyancy sorting" can lead to a selection bias in Paluch diagrams; buoyant parcels are more likely to come from below and negatively buoyant parcels from above, explaining the alignment of data. Consistent with this idea, more recent modeling work (e.g., Heus et al. 2008; Boing et al. 2014) reproduced the observed Paluch diagrams but indicated the dominant role of lateral mixing based on a Lagrangian particle-tracking analysis.

are equivalent to steady-state entraining-plume solutions for $C_{\mathrm{Tr},z}$ with z interpreted as height within the plume. However, it is emphasized that this scaling only applies near the HMB, and not lower in the updraft, which is a key difference from the standard entraining-plume model.

b. Turbulent entrainment of buoyancy

Most convection schemes solve equations for conserved or approximately conserved quantities such as total water and moist static energy. Such an approach could be employed here to derive an equation for B, but this gives large errors using a linearized form of dq_s/dT (q_s is the saturation vapor mixing ratio and T is temperature) needed to relate moist static energy and q_s. Thus, numerical integration appears to be required for reasonably accurate solutions using this approach. However, since we seek understanding of updraft behavior by deriving analytic solutions, an alternative approach is instead used to estimate B. Noting that $q_v \approx q_s$ within cloudy updrafts implies that $S = q_v - q_s = 0$ and hence $dS/dt = 0$, where S is the absolute supersaturation. The supersaturation equation can be expanded and expressed in terms of the condensation rate C_D to give

$$\frac{dS}{dt} = \left(\frac{dq_v}{dt}\right)_{\mathrm{mix}} - \left(\frac{dq_s}{dt}\right)_{\mathrm{mix}} + \frac{gw}{c_p}\frac{dq_s}{dT} - C_D - \frac{L_v}{c_p}\frac{dq_s}{dT}C_D = 0, \tag{12}$$

where subscript "mix" indicates the time rate of change due to turbulent mixing, and the effects of other diabatic processes (e.g., radiation) are neglected. Here g, c_p, and L_v are the acceleration of gravity, specific heat of air at constant pressure, and latent heat of vaporization, respectively.

For horizontal turbulent mixing of a saturated updraft and subsaturated environmental air, we use (8) with $C_{\mathrm{Tr},E} = q_{vE}$ (vapor mixing ratio of the environment) in the environment and $C_{\mathrm{Tr}} = q_v = q_s$ in the updraft. This gives

$$\left(\frac{dq_v}{dt}\right)_{\mathrm{mix}} = -\frac{2k^2 Lw(q_s - q_{vE})}{P_r R^2}. \tag{13}$$

An expression for $(dq_s/dt)_{\mathrm{mix}}$ is derived from the equation for horizontal mixing of temperature combined with linearizing $dq_s/dT \approx (q_s - q_{sE})/(T - T_E)$, where q_{sE} is the saturation mixing ratio of the environment and T and T_E are the updraft temperature and environmental temperature, respectively. This approximation is valid since horizontal temperature differences between the updraft and the environment are small relative to the temperature itself. For isobaric mixing of temperature $(dT/dt)_{\mathrm{mix}}$, we use (8) with $C_{\mathrm{Tr},E} = T_E$ in the environment and $C_{\mathrm{Tr}} = T$ in the updraft. Combined with the linearized dq_s/dT, this gives

$$\left(\frac{dq_s}{dt}\right)_{\mathrm{mix}} = \frac{dq_s}{dT}\left(\frac{dT}{dt}\right)_{\mathrm{mix}} \approx -\frac{2k^2 Lw(q_s - q_{sE})}{P_r R^2}. \tag{14}$$

Combining (12)–(14) and rearranging terms gives an expression for condensation rate that includes vertical motion and turbulent mixing of temperature and water vapor:

$$C_D = \frac{gw}{c_p \Gamma}\frac{dq_s}{dT} - \frac{2k^2 Lw(q_{sE} - q_{vE})}{P_r R^2 \Gamma}, \tag{15}$$

where $\Gamma = 1 + (L_v/c_p)(dq_s/dT) \approx 1 + L_v^2 q_s/(c_p R_v T^2)$ is a thermodynamic parameter ranging from ~1.5 to 2.5 for typical atmospheric conditions, with dq_s/dT estimated using the Clausius–Clapeyron relationship; R_v is the gas constant for water vapor. The condensation rate can be expressed in terms of a buoyancy tendency by noting $dB/dt = L_v g C_D/(c_p T_E)$, neglecting condensate loading, water vapor, and pressure perturbation effects on B. When combined with (15) and including the direct lateral turbulent mixing of buoyancy, this gives

$$\frac{dB}{dt} = \frac{L_v g}{c_p T_E}\left[\frac{gw}{c_p \Gamma}\frac{dq_s}{dT} - \frac{2k^2 Lw(q_{sE} - q_{vE})}{P_r R^2 \Gamma}\right] - \frac{2k^2 LwB}{P_r R^2}. \tag{16}$$

This equation can be simplified by expressing the first term on the right-hand side, which represents the buoyancy tendency from moist pseudoadiabatic ascent, in terms of the difference between the pseudoadiabatic and environmental lapse rates Q multiplied by g/T_E to give

$$\frac{dB}{dt} = gQw - \frac{2L_v g k^2 Lw(q_{sE} - q_{vE})}{c_p T_E P_r R^2 \Gamma} - \frac{2k^2 LwB}{P_r R^2}. \tag{17}$$

Taking (17) as the material derivative, applying the chain rule similar to the approach for C_{Tr} in section 2a, and dividing by w gives

$$\frac{dB}{dz} = gQ - \frac{2L_v g k^2 Lq_{sE}(1 - R_H)}{c_p T_E P_r R^2 \Gamma} - \frac{2k^2 LB}{P_r R^2}, \tag{18}$$

where environmental relative humidity $R_H = q_{vE}/q_{sE}$.

For constant gQ, T, and R_H, (18) can be solved analytically for $B(z)$ by a separation of variables if B is specified at the lower boundary (the LFC). However,

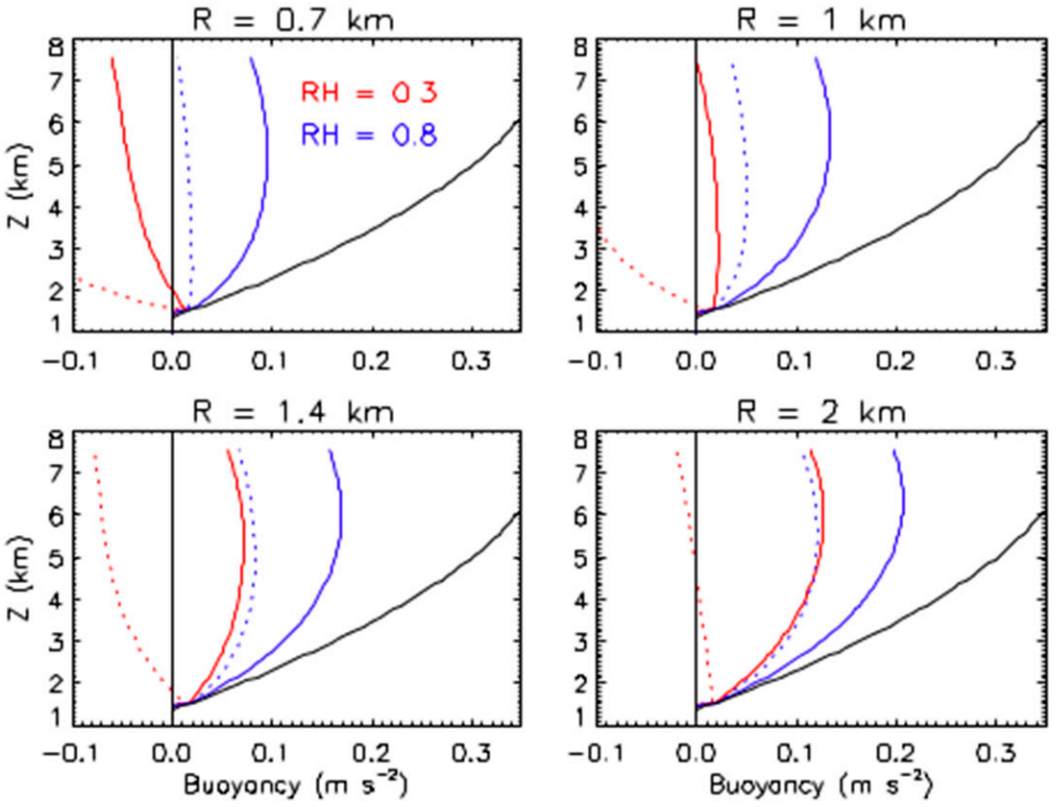

FIG. 1. Vertical profiles of the analytic buoyancy at the updraft center and at the HMB following (23) (solid lines) and that between the LFC and HMB with enhanced lateral turbulent mixing following (32) (dotted lines) for various updraft radii R. Environmental relative humidity R_H is 0.3 (red) or 0.8 (blue). The value of k^2/P_r for the calculations is 0.2. Black lines indicate the pseudoadiabatic buoyancy calculated from ascent of the most energetic parcel using the thermodynamic sounding of Weisman and Klemp (1982).

given that these quantities generally vary with height, integration of (18) from the LFC to z is written more generally as

$$B = \int_{\mathrm{LFC}}^{z} \left[gQ - \frac{2L_v g k^2 L q_{sE}(1 - R_H)}{c_p T_E P_r R^2 \Gamma} - \frac{2k^2 LB}{P_r R^2} \right] dz. \tag{19}$$

An expression for the pseudoadiabatic buoyancy B_{AD} is given by setting $k = 0$ in (19) to yield

$$B_{\mathrm{AD}} = \int_{\mathrm{LFC}}^{z} gQ\, dz. \tag{20}$$

Combining (19) and (20) yields

$$B = B_{\mathrm{AD}} + \int_{\mathrm{LFC}}^{z} \left[-\frac{2L_v g k^2 L q_{sE}(1 - R_H)}{c_p T_E P_r R^2 \Gamma} - \frac{2k^2 LB}{P_r R^2} \right] dz. \tag{21}$$

The integral in (21) is approximated by assuming a linear vertical profile of B between the LFC and z. This gives

$$B = B_{\mathrm{AD}} - \frac{2L_v g k^2 Lz}{c_p P_r R^2} \Phi - \frac{k^2 LzB}{P_r R^2}, \tag{22}$$

where $\Phi = (1/z)\int_{\mathrm{LFC}}^{z} \{[q_{sE}(1 - R_H)]/(\Gamma T_E)\}\, dz$ is a vertically averaged (from the LFC to z) environmental thermodynamic parameter that depends on T_E and R_H. Rearranging terms in (22) gives an estimate for B at the updraft center:

$$B = \frac{B_{\mathrm{AD}}}{1 + k^2 Lz/(P_r R^2)} - \frac{2L_v g k^2 L \Phi}{c_p (P_r R^2/z + k^2 L)}. \tag{23}$$

The first term on the right-hand side of (23) represents the direct dilution of buoyancy, while the second term represents dilution caused by turbulent entrainment of dry air. Figure 1 shows B (solid red and blue lines) calculated from (23) as a function of z for different values of R and R_H. We calculate B_{AD} from pseudoadiabatic

ascent of the most unstable parcel using the thermodynamic sounding from Weisman and Klemp (1982), modified so that R_H above the LFC (~1.5-km height) is constant to isolate the effects of R_H, while $k^2/P_r = 0.2$ and $L = R$. Strong sensitivity to both R and R_H is evident, with B going negative about 500 m above the LFC for a narrow updraft ($R = 0.7$ km) in a dry environment ($R_H = 0.3$).

c. Updraft vertical velocity

Performing a Reynolds averaging of the Boussinesq vertical momentum equation, neglecting the vertical turbulent flux divergence, and following the approach in section 2a to estimate $\overline{u'w'}$ similar to $\overline{u'C'_{\rm Tr}}$, gives

$$\frac{dw}{dt} = -\frac{1}{\rho_0}\frac{\partial p}{\partial z} - \frac{2k^2Lw^2}{R^2} + B, \tag{24}$$

where p is air pressure and all quantities except air density ρ_0 are perturbations from a hydrostatic, motionless basic state. The first term on the right-hand side is the vertical perturbation pressure gradient force, the second term is the turbulent mixing of w, and the third term is the buoyant acceleration of w. Morrison (2016a,b) and Peters (2016) discuss the perturbation pressure term in detail. These papers derive analytic scalings for this term as a function of R and the updraft height H.

An expression for dw/dt is derived by combining (24) and the expression for B from (23), giving

$$\frac{dw}{dt} = -\frac{1}{\rho_0}\frac{\partial p}{\partial z} - \frac{2k^2Lw^2}{R^2} + \frac{B_{\rm AD}}{1 + k^2Lz/(P_rR^2)} - \frac{2L_v g k^2 L\Phi}{c_p(P_rR^2/z + k^2L)}. \tag{25}$$

Again we take (25) as a material derivative, use the chain rule with $w = dz/dt$, and integrate from the LFC to z assuming a linear vertical profile of w so that $\int_{\rm LFC}^{z} w^2\,dz' \approx (w^2/z^2)\int_{\rm LFC}^{z} z'^2\,dz' = w^2z/3$. Combined with the analytic expression for $\int_{\rm LFC}^{z}(1/\rho_0)(\partial p/\partial z)\,dz'$ from Morrison [2016a, his (20) therein] this yields, after rearranging terms to solve for w,

$$w = \left[\frac{2\text{CAPE}([1/z^2 - L_v g k^2 L\Phi/(c_p P_r R^2\text{CAPE})]\{P_rR^2z/(k^2L) - [P_r^2R^4/(k^4L^2)]\ln[k^2Lz/(P_rR^2) + 1]\})}{1 + \alpha^2R^2/H^2 + 4k^2Lz/(3R^2)}\right]^{1/2}, \tag{26}$$

where CAPE is the convective available potential energy found by integrating the buoyancy from the LFC to height z, and α is a parameter in the perturbation pressure term equal to the ratio of the vertical velocity at the updraft center to that horizontally averaged across the updraft (Morrison 2016a).

Turbulent mixing and perturbation pressure effects both reduce w from the maximum thermodynamic value for a nonentraining parcel (i.e., $w_{\rm max} = \sqrt{2\text{CAPE}}$). In the denominator of (26), the second term represents the effects of perturbation pressure, and the third term is the direct turbulent mixing of vertical momentum. Terms in the numerator represent the turbulent mixing of buoyancy and dry air.

Figure 2 shows w calculated using (26), again assuming $k^2/P_r = 0.2$ and $L = R$ and using the modified thermodynamic sounding from Weisman and Klemp (1982), as a function of R for various $z = H$ (Fig. 2a) and as a function of R_H (Fig. 2b). The behavior of w as a function of R is interesting, since w decreases with increasing R from perturbation pressure effects, but also decreases with decreasing R from lateral turbulent mixing. This leads to a peak w occurring in an intermediate range of R between ~1 and 5 km. [It is important to keep in mind that the w in (26) is from the organized convective-scale motion and does not directly include turbulent-scale fluctuations of w.] This behavior is consistent with previous numerical results of Holton (1973) and Kuo and Raymond (1980). Here the value of R at which this occurs $R_{\rm peak}$ increases with z. The value of $R_{\rm peak}$ does not depend directly on CAPE, although it is affected by the entrainment of dry air such that a drier environment favors a larger $R_{\rm peak}$. Overall, the maximum w over the range of R is about one-half the value of $w_{\rm max}$. Here $L = R$ was chosen for simplicity and based on LES of moist deep convection showing a lack of scale separation in the w kinetic energy spectra between updraft-scale eddies and smaller-scale turbulent eddies (Moeng et al. 2009; Lebo and Morrison 2015). Decreasing L, for example to a value of $R/2$, decreases the effects of entrainment and shifts $R_{\rm peak}$ to smaller values (not shown) but does not change the general picture.

d. The effects of dynamic entrainment

Dynamic entrainment caused by organized lateral inflow of environmental air between the LFC and HMB, required by mass continuity to balance vertical acceleration of updraft air, directly affects quantities away

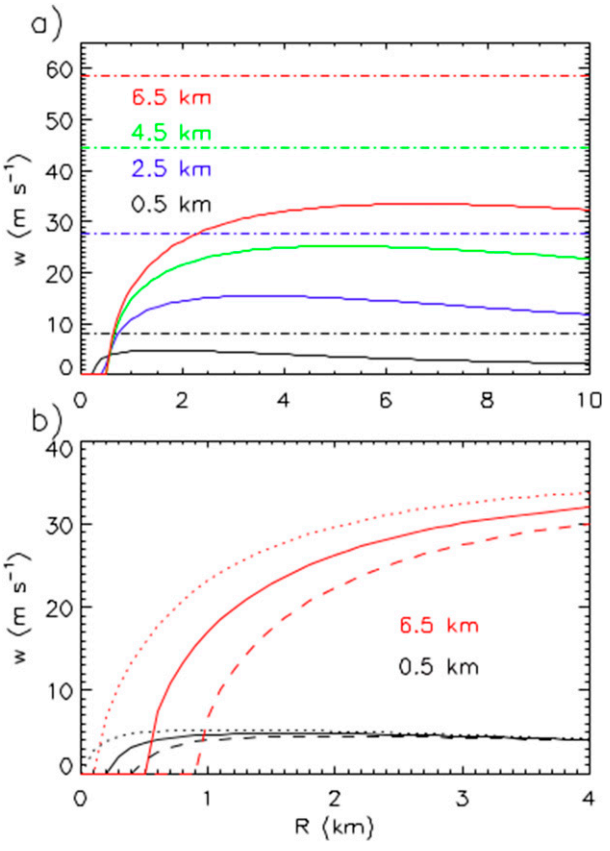

FIG. 2. Analytic vertical velocity w at the updraft center and at the height of maximum buoyancy calculated using (26) as a function of updraft radius R. Values of w at varying heights are indicated by colored lines. (a) Results for $R_H = 0.5$, with the thermodynamic maximum w equal to $\sqrt{2\text{CAPE}}$ indicated by horizontal dotted–dashed lines and the calculated w from (26) indicated by solid lines. CAPE is calculated by vertically integrating the pseudoadiabatic buoyancy from the LFC to the given height. (b) Results for $R_H = 0.1$ (dashed lines), 0.5 (solid lines), and 0.9 (dotted lines). Values of k^2/P_r and P_r are 0.2 and $\frac{1}{3}$, respectively.

from the updraft center. If mixing between entrained environmental air and buoyant updraft air is relatively slow compared to the entrainment rate and/or the environment is dry, then one may expect the mixture of entrained and updraft air to become negatively buoyant and experience downward acceleration, in effect being detrained from the updraft and hence reducing R. This is essentially the buoyancy sorting mechanism (e.g., Raymond and Blyth 1986), which is believed to play an important role in the dynamics of moist convection. On the other hand, if the entrained air is humid and/or rapidly mixed with updraft air, then dynamic entrainment will lead to the dilution of updraft properties but not necessarily a reduction of R. An additional complication is the recirculation of air detrained from the updraft, so that the entrained air along the lateral updraft edges may negatively buoyant, descending, and moist relative to the environment (Heus and Jonker 2008).

Since dynamic entrainment has no direct impact at the updraft center owing to symmetry of the flow ($u = 0$ at $r = 0$), the dilution of updraft properties away from the updraft center and/or narrowing of updrafts via buoyancy sorting implies a sharpening of horizontal gradients across the updraft. This in turn enhances lateral mixing from smaller-scale turbulence. Thus, it is argued that dynamic entrainment and turbulent entrainment are inextricably linked through changes in horizontal heterogeneity of properties across the updraft. This is intuitive since the separation of dynamic and turbulent entrainment is inherently artificial; kinetic energy spectra from LES of moist deep convection show no evidence for a scale separation between updraft-scale motion and smaller-scale turbulence (Moeng et al. 2009; Lebo and Morrison 2015). This interlinkage between the sharpening of gradients associated with buoyantly driven updraft-scale eddies and mixing by smaller-scale turbulent eddies is consistent with the picture put forth by Grabowski and Clark (1993) explaining the dynamics of the cloud–environment interface.

The sharpening of horizontal gradients from dynamic entrainment is estimated from the advective form of the scalar conservation equation using an upstream horizontal finite differencing, similar to that used by Asai and Kasahara (1967) and de Rooy and Siebesma (2010):

$$\frac{\partial C_{\mathrm{Tr},U}}{\partial t} = -\frac{u_U(C_{\mathrm{Tr},B} - C_{\mathrm{Tr},U})}{\Delta r} - w_U\frac{\partial C_{\mathrm{Tr},U}}{\partial z} = -\frac{2u_U(C_{\mathrm{Tr},B} - C_{\mathrm{Tr},U})}{R_{\mathrm{HMB}}} - w_U\frac{\partial C_{\mathrm{Tr},U}}{\partial z}, \quad (27)$$

where R_{HMB} is the updraft radius at the height of maximum buoyancy, $\Delta r = R_{\mathrm{HMB}}/2$ is the horizontal spacing, and subscripts U and B denote values within the updraft and at the lateral boundary, respectively (Fig. 3). Interpreting $C_{\mathrm{Tr},U}$ as an average value of C_{Tr} between $r = 0$ and $r = R_{\mathrm{HMB}}$, either a reduction of R or dilution of local updraft properties reduces $C_{\mathrm{Tr},U}$ from dynamic entrainment below the HMB. Thus, no explicit assumptions are made about the role of buoyancy sorting in sharpening horizontal gradients between $r = 0$ and $r = R_{\mathrm{HMB}}$.

Assuming a linear horizontal profile of u such that $u_U \sim u_B/2$ (since $u = 0$ at $r = 0$) and with $C_{\mathrm{Tr},B} = 0$, (27) is expressed as

$$\frac{\partial C_{\mathrm{Tr}}}{\partial t} = \frac{u_B C_{\mathrm{Tr},U}}{R_{\mathrm{HMB}}} - w_U\frac{\partial C_{\mathrm{Tr},U}}{\partial z}. \quad (28)$$

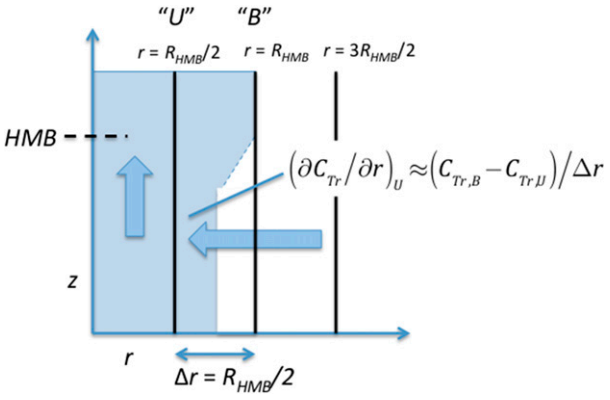

FIG. 3. Diagram of the horizontal discretization applied to the scalar conservation equation to estimate the effects of dynamic entrainment. HMB is the height of maximum buoyancy and $R_{\rm HMB}$ is the updraft radius at the HMB.

The first term on the right-hand side of (28) is the dynamic entrainment of $C_{{\rm Tr},U}$ due to organized convective flow, and u_B is given by the horizontally averaged mass continuity equation, yielding after rearranging terms

$$u_B = -\frac{R_{\rm HMB}}{2}\frac{\partial\langle w\rangle}{\partial z}, \tag{29}$$

where $\langle w\rangle$ is the vertical velocity horizontally averaged from $r = 0$ to $r = R_{\rm HMB}$.

Combining (28) and (29) and approximating $\langle w\rangle \sim w_U$ gives

$$\frac{\partial C_{\rm Tr}}{\partial t} = -\frac{\partial w_U}{\partial z}\frac{C_{{\rm Tr},U}}{2} - w_U\frac{\partial C_{{\rm Tr},U}}{\partial z}. \tag{30}$$

Following the material derivative of upward-moving parcels below the HMB (or equivalently assuming steady state below the HMB), approximating $\partial w_U/\partial z \sim w_U/z$ and $\partial C_{{\rm Tr},U}/\partial z \sim (C_{{\rm Tr},U} - C_{{\rm Tr},0})/z$ with the conditions that $w_U = 0$ and $C_{{\rm Tr},U} = C_{{\rm Tr},0}$ at the LFC, dividing by w_U, and rearranging terms gives

$$C_{{\rm Tr},U} \sim \frac{2}{3}C_{{\rm Tr},0}. \tag{31}$$

Since dynamic entrainment has no direct impact on quantities at the updraft center, the implication is that all being else equal it increases horizontal gradients between the updraft center and $r = R_{\rm HMB}/2$ by a factor of ~3/2, independent of w, $R_{\rm HMB}$, or z. This simple scaling therefore suggests an increase in lateral turbulent mixing by $(3/2)^2 = 9/4$, since mixing is related to the product of horizontal gradients of $C_{\rm Tr}$ and w (assuming a similar 3/2 scaling of w gradients from dynamic entrainment). Thus, an estimate of $C_{\rm Tr}$ at the updraft center in the dynamic entrainment region between the LFC and HMB is given by (11) but with a scaling of the turbulent mixing by 9/4.

In this derivation it is assumed that the region with $C_{{\rm Tr},B} > 0$ defines the radius $R_{\rm HMB}$, so that $C_{{\rm Tr},B} = 0$. This implicitly accounts for the detrainment of $C_{\rm Tr}$ into the environment (assuming $C_{\rm Tr} = 0$ in the environment), increasing the width of the region of nonzero $C_{\rm Tr}$. However, the situation is more complicated for buoyancy and vertical velocity because detrainment of cloud water and its subsequent evaporation can lead to a negatively buoyant, moist, descending shell along the lateral updraft edge (Heus and Jonker 2008; Jonker et al. 2008; de Rooy et al. 2013). Thus, air recirculated and entrained into the updraft may have $B < 0$ and $w < 0$ as well as R_H greater than in the surrounding environment. Nonetheless, given the lack of a theoretical framework for describing the properties of the moist descending shell, for simplicity it is assumed that entrained air has $B = 0$ and R_H equal to that of the environment, and the region with $B > 0$ and $w > 0$ defines $R_{\rm HMB}$. With these assumptions, an estimate of B at the updraft center between the LFC and HMB is given by applying the 9/4 scaling to the turbulent mixing terms in (23) to yield

$$B = \frac{B_{\rm AD}}{1 + 9k^2Lz/(4P_rR_{\rm HMB}^2)} - \frac{9L_vgk^2L\Phi}{2c_p(P_rR_{\rm HMB}^2/z + 9k^2L/4)}, \tag{32}$$

where z is the height above the LFC (between the LFC and HMB), in contrast to (23) where z is the height of maximum buoyancy as it rises over time.

Values of B calculated using (32) are shown in Fig. 1, using the same sounding and setup described in section 2b. Certain combinations of $R_{\rm HMB}$, z, and R_H lead to $B < 0$ between the LFC and HMB (dotted lines) via (32) but $B > 0$ at the HMB (solid lines) via (23). This implies that dynamic entrainment, by enhancing smaller-scale turbulent mixing relative to that at the HMB, can lead to the region of positive buoyancy at the HMB being cut off from the LFC by a region with $B < 0$ between the LFC and HMB. In other words, this suggests that under certain conditions updrafts will exhibit a structure that resembles rising thermals instead of plumes connected to the LFC by a continuous region of positive buoyancy. Based on (32), updraft structure will tend to be more thermal-like than plume-like when $R_{\rm HMB}$ is small, the environment is dry, and when the distance from

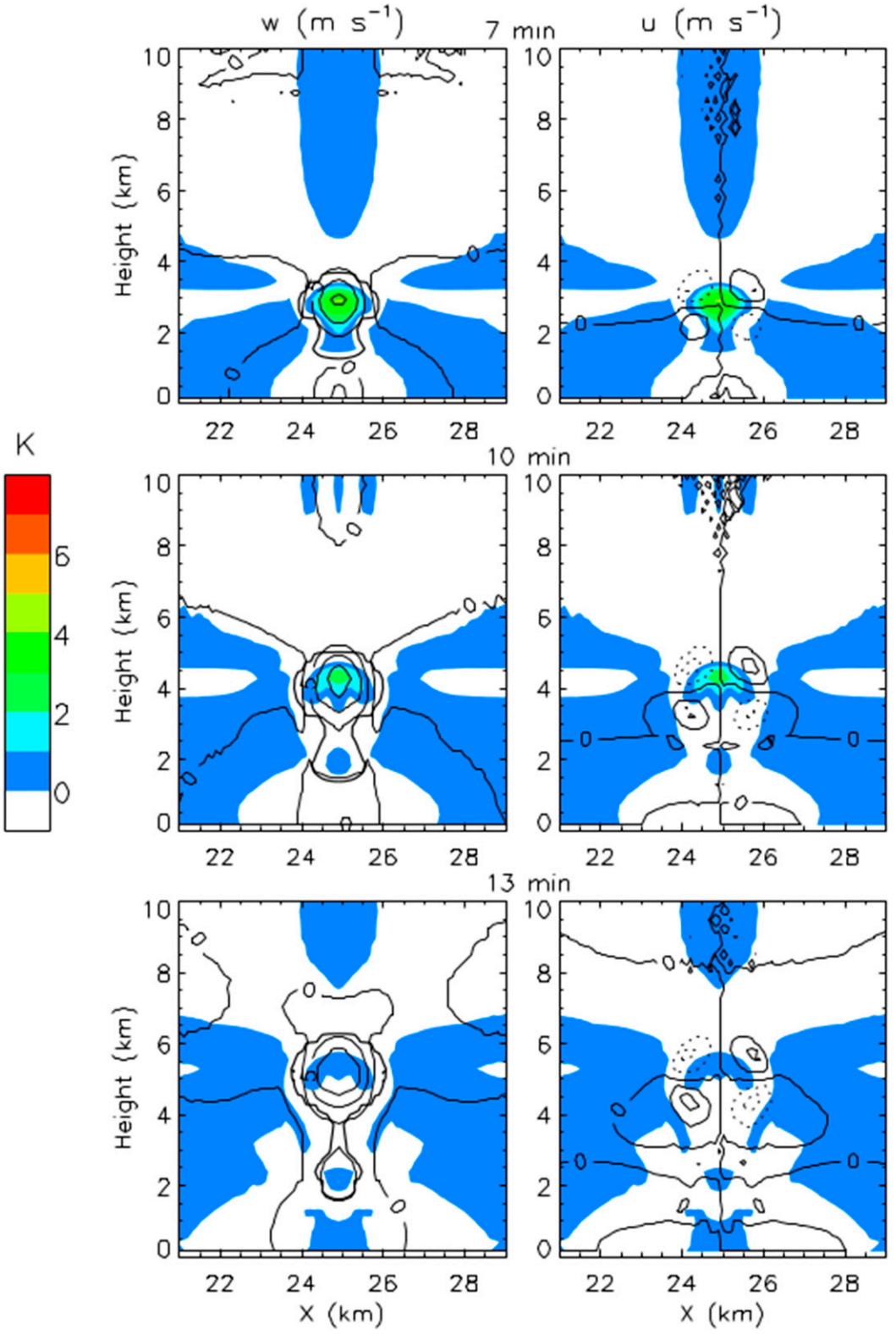

FIG. 4. Vertical cross-sectional plots of perturbation potential temperature (color contours), relative to the (left) horizontal-domain-average vertical air velocity w, and (right) horizontal air velocity u, for the simulation with environmental $R_H = 0.425$ and a 1-km initial bubble. The contour interval is 5 m s^{-1} for w and 2 m s^{-1} for u. Results are shown at t = (top) 7, (middle) 10, and (bottom) 13 min. Only a small portion of the model domain is shown.

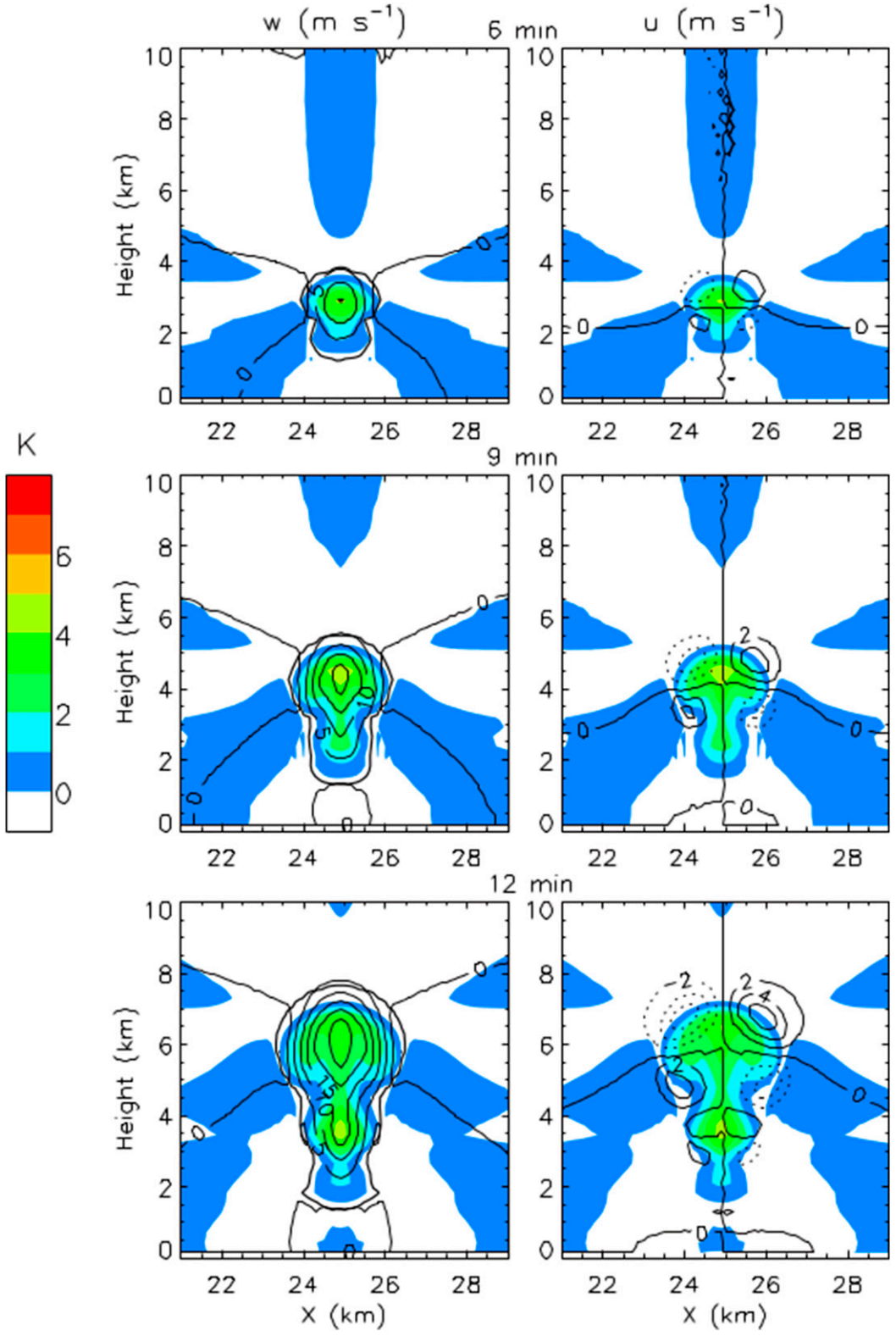

FIG. 5. As in Fig. 4, but for the simulation with $R_H = 0.85$ and $t =$ (top) 6, (middle) 9, and (bottom) 12 min.

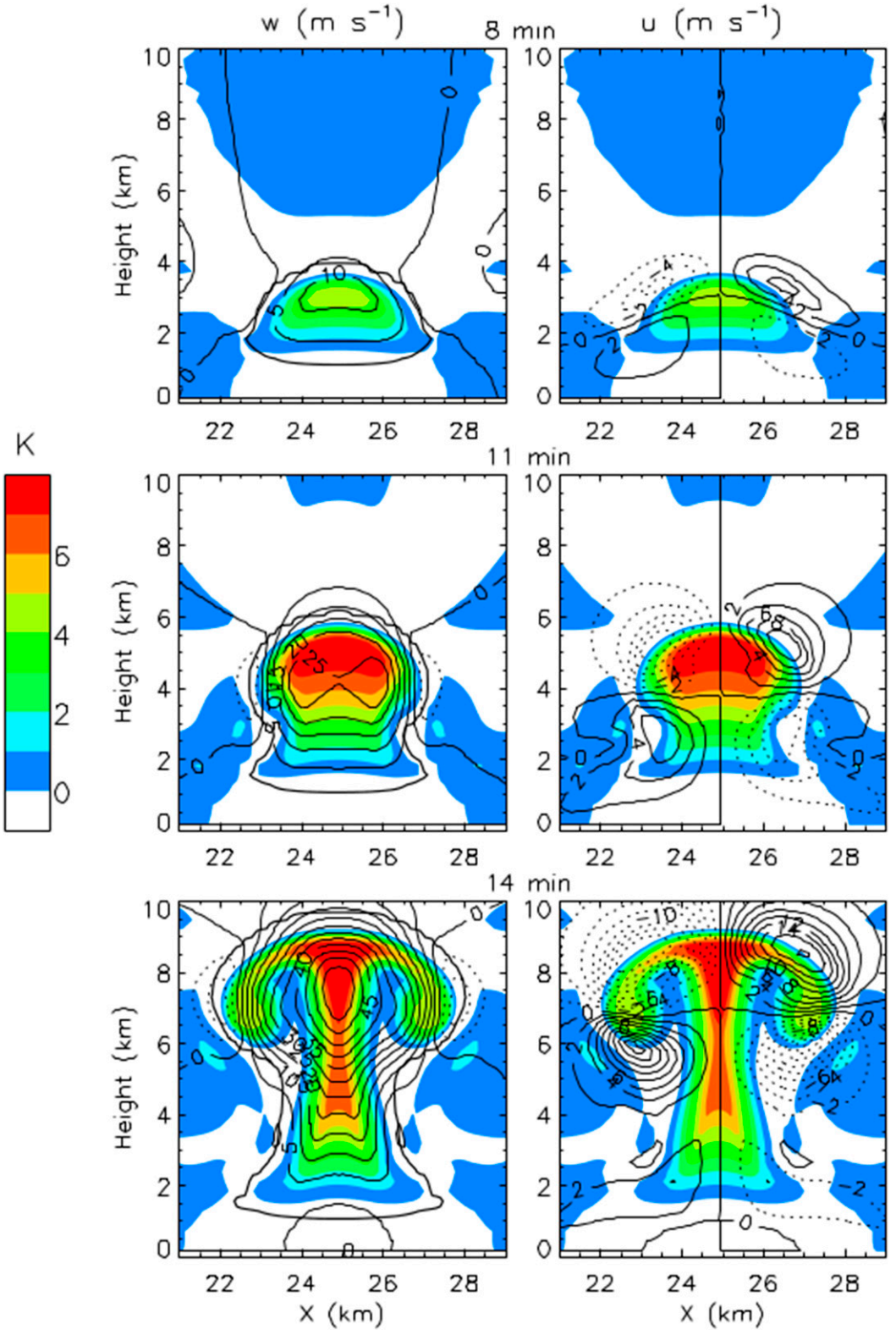

FIG. 6. As in Fig. 4, but for the simulation with $R_H = 0.425$ and a 4-km initial bubble at $t =$ (top) 8, (middle) 11, and (bottom) 14 min.

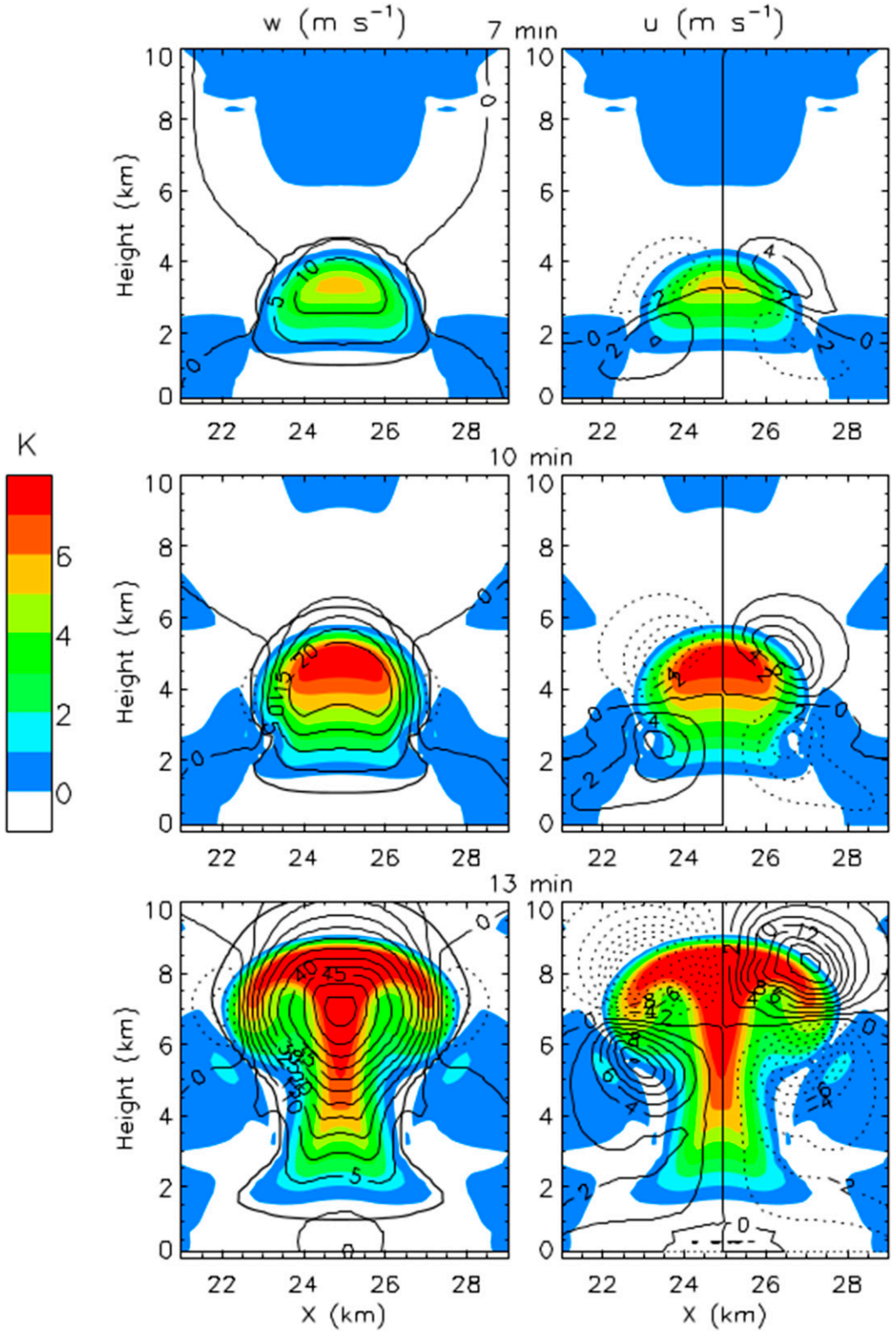

FIG. 7. As in Fig. 4, but for the simulation with $R_H = 0.485$ and a 4-km initial bubble, and $t =$ (top) 7, (middle) 10, and (bottom) 13 min.

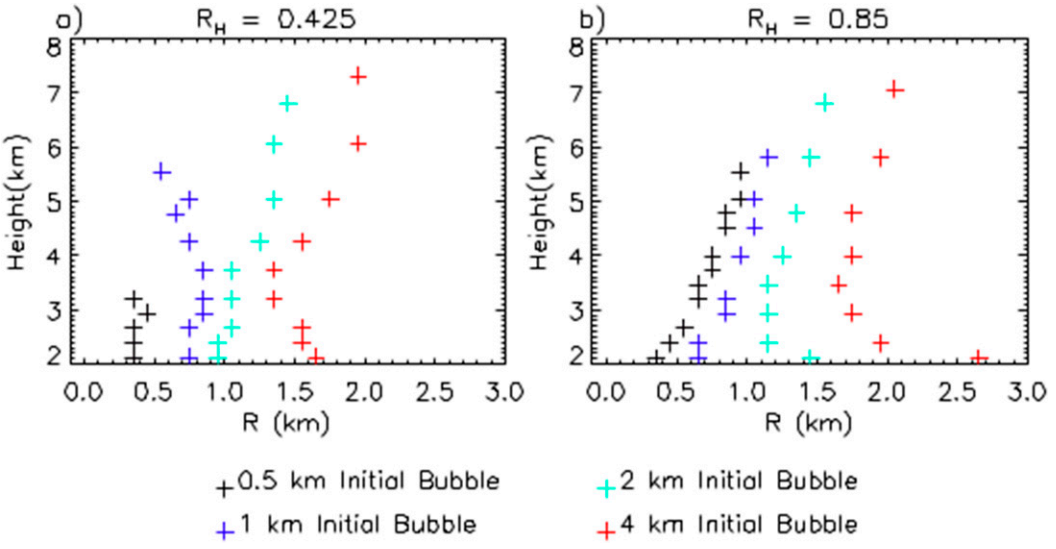

FIG. 8. Updraft radius R at the height of maximum buoyancy as it rises over time from the simulations with R_H = (a) 0.425 and (b) 0.85 and varying initial bubble radii. Individual data points are plotted at 1-min intervals. The updraft radius is defined by the continuous region with $w > 0$ and $B > 0$, where B is calculated relative to the horizontal domain-average buoyancy.

the HMB to LFC is large. This is an important distinction with the standard entraining-plume model, which does not explicitly link smaller-scale turbulent mixing to the larger-scale organized convective flow.

Similarly to B, w at the updraft center between the LFC and HMB is estimated by assuming the entrained air has $w = 0$, $B = 0$, and R_H equal to that of the environment. Applying the 9/4 scaling to the turbulent mixing terms in (26) gives

$$w = \left[\frac{2\mathrm{CAPE}([1/z^2 - 9L_v g k^2 L\Phi/(4c_p P_r R_{\mathrm{HMB}}^2 \mathrm{CAPE})]\{4P_r R_{\mathrm{HMB}}^2 z/(9k^2 L) - 16P_r^2 R_{\mathrm{HMB}}^4/(81k^4 L^2)\ln[9k^2 Lz/(4P_r R_{\mathrm{HMB}}^2) + 1]\})}{1 + \alpha^2 R_{\mathrm{HMB}}^2/H^2 + 3k^2 Lz/R_{\mathrm{HMB}}^2}\right]^{1/2}. \quad (33)$$

3. Idealized numerical simulations

a. Model description and setup

To assess the theoretical expressions derived in section 2, numerical simulations were performed using the Weather Research and Forecasting (WRF) Model, version 3.6.1 (Skamarock et al. 2008). WRF is a compressible, nonhydrostatic atmospheric model. For simplicity and to allow a direct comparison with the theoretical expressions, effects of condensate loading on the buoyancy are neglected. Fifth-order horizontal advection and third-order vertical advection with a limiter to ensure positive definiteness for nonmomentum quantities are used.

The model is three-dimensional (3D) with a domain extending 50 km in each horizontal direction and 20 km vertically and 100-m horizontal grid spacing and approximately 250-m vertical grid spacing. Additional tests were performed with higher vertical resolution, ~100-m grid spacing, so that the grid aspect ratio was approximately 1:1. These tests show only small differences in the structure and evolution of the updrafts compared to the coarser-resolution simulations, including the buoyancy and vertical velocity fields, and hence the main results and conclusions are not affected. Lateral boundary conditions are periodic, with free-slip conditions at the surface. A Rayleigh damper with damping coefficient of 0.003 s^{-1} is applied to the upper 5 km to limit spurious wave reflection. All physical parameterizations except microphysics are neglected for simplicity; for microphysics, only cloud water condensation and evaporation are considered using the scheme of Morrison et al. (2009).

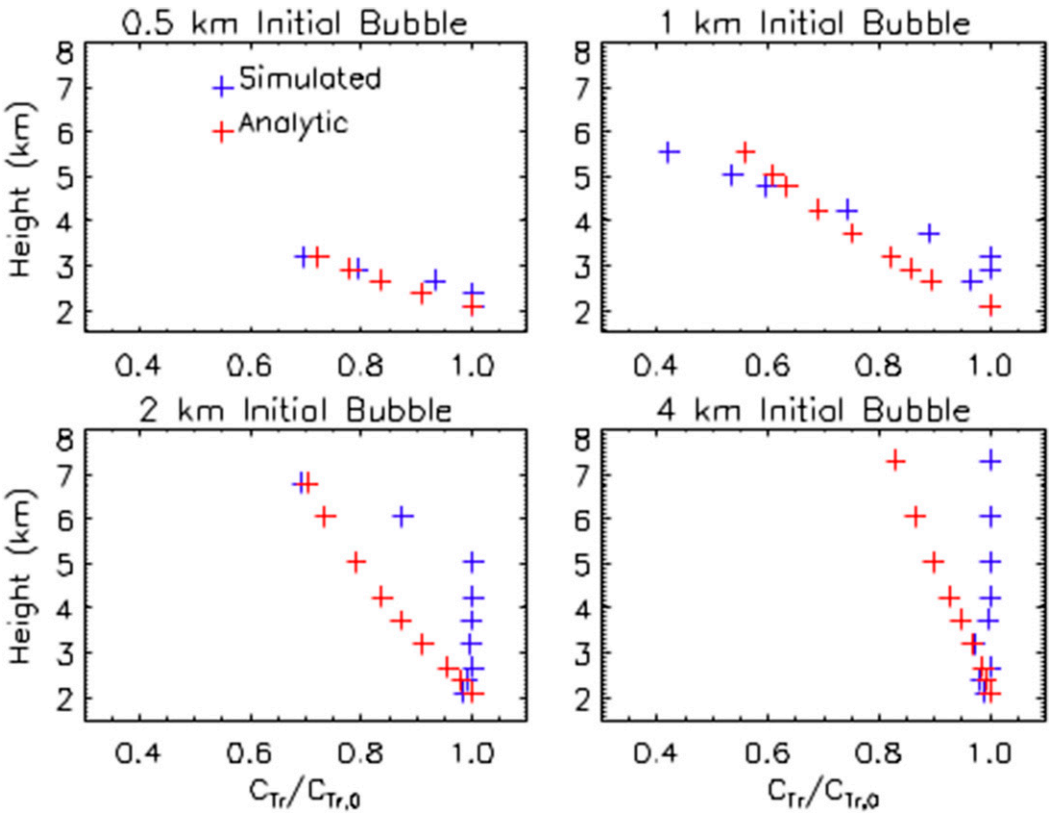

FIG. 9. The ratio $C_{Tr}/C_{Tr,0}$ at the updraft center and height of maximum buoyancy as it rises over time from the numerical simulations (blue) and analytic solutions (red) calculated using (11). Results are shown for $R_H = 0.425$ and varying initial bubble radii as indicated. Individual data points are plotted at 1-min intervals.

Initial conditions are unsheared with horizontally homogeneous thermodynamic profiles, except for a single warm bubble applied in each simulation to initiate convection. The size of the initial warm bubble varies among simulations, with a cosine dependence on the shape of the perturbation potential temperature (θ') profiles and a maximum θ' of 2 K in the bubble center. Initial bubble radii of 0.5, 1, 2, and 4 km are tested. The bubbles have a height of 2 km centered at an altitude of 1.5 km. The initial thermodynamic sounding follows from the analytic sounding of Weisman and Klemp (1982). However, to more tightly control the impact of environmental R_H, the sounding is modified so that it is constant above 2 km, set to either 0.425 or 0.85. The R_H below 2 km is the same as in the original Weisman–Klemp sounding to keep approximately the same LFC (~1.5 km).

A first-order mixing scheme (Smagorinsky 1963) is applied to represent the effects of subgrid-scale eddies. Explicitly resolved turbulence is limited in these simulations because of the finite spinup time required to develop grid-scale turbulent motion and an energy cascade (e.g., Chow et al. 2005; Lebo and Morrison 2015). To better represent the mixing expected in a turbulent convective cloud, the subgrid-scale mixing length, which is typically equal to the model grid length Δx or filter cutoff scale in LES, was increased by a factor of 5–500 m compared to the 100-m horizontal grid spacing. Thus, it is emphasized that these simulations are not LES as it is typically defined, and instead should be viewed as high-resolution simulations of a diffusive growing moist bubble. This particular scaling of the mixing length was chosen so that the overall mixing is dominated by the more controlled parameterized subgrid-scale mixing as opposed to the implicit numerical mixing, since it has been shown in a model with similar numerics that numerical mixing dominates at scales smaller than about 5–6Δx (Skamarock 2004). While simple, this setup allows for a straightforward analysis and comparison with the theoretical expressions since 1) horizontal symmetry around the central bubble axis is (nearly) retained, 2) the updraft size is well controlled by the initial bubble size so that the effects of varying updraft size can be tested systematically, and 3) mixing is mainly controlled by a specified mixing length. Additional simulations were performed with the mixing length set to Δx (100 m)

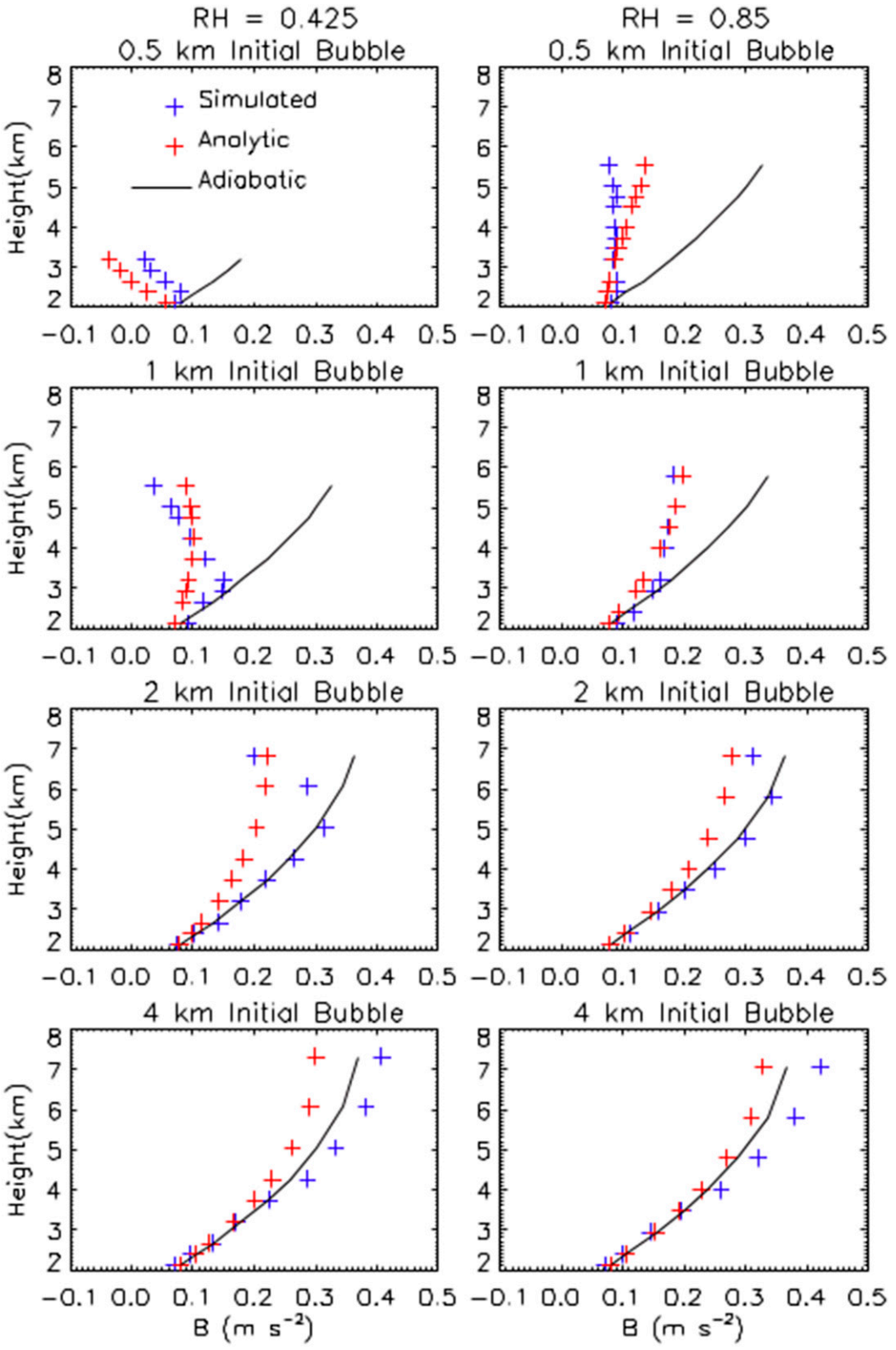

FIG. 10. Buoyancy at the updraft center and height of maximum buoyancy as it rises over time from the numerical simulations (blue) and analytic solution (red) calculated using (23). Results are shown for R_H = (left) 0.425 and (right) 0.85, with varying initial bubble radii as indicated. Individual data points are plotted at 1-min intervals. The pseudoadiabatic buoyancy is shown by the black solid line.

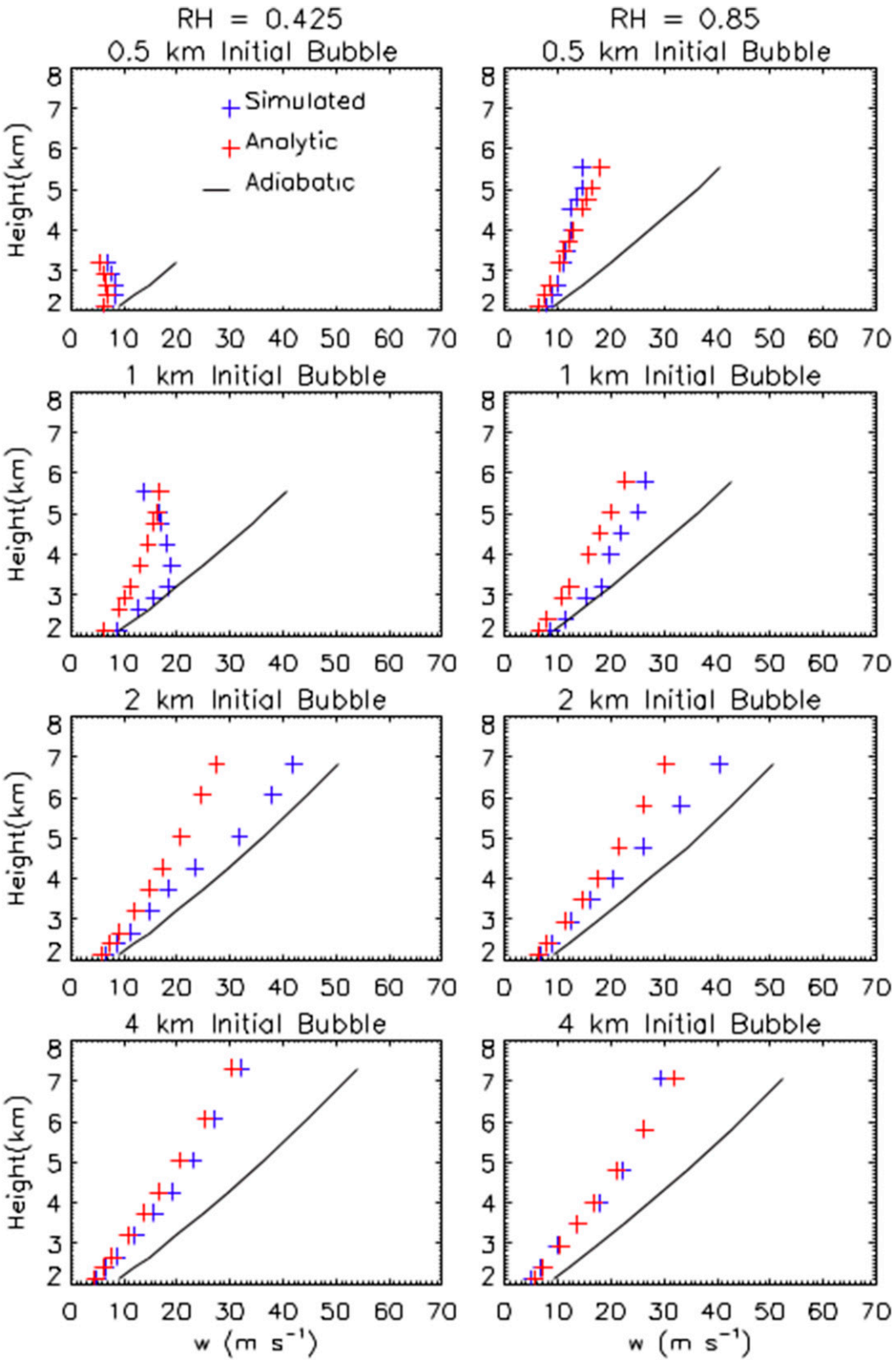

FIG. 11. Vertical velocity at the updraft center and height of maximum buoyancy as it rises over time from the numerical simulations (blue) and analytic solutions (red) calculated using (26). Results are shown for R_H = (left) 0.425 and (right) 0.85, with varying initial bubble radii as indicated. Individual data points are plotted at 1-min intervals. The thermodynamic maximum vertical velocity neglecting entrainment and perturbation pressure effects, equal to $\sqrt{2\text{CAPE}}$, is shown by the black solid line. CAPE is calculated by vertically integrating the pseudoadiabatic buoyancy from the LFC to the given height.

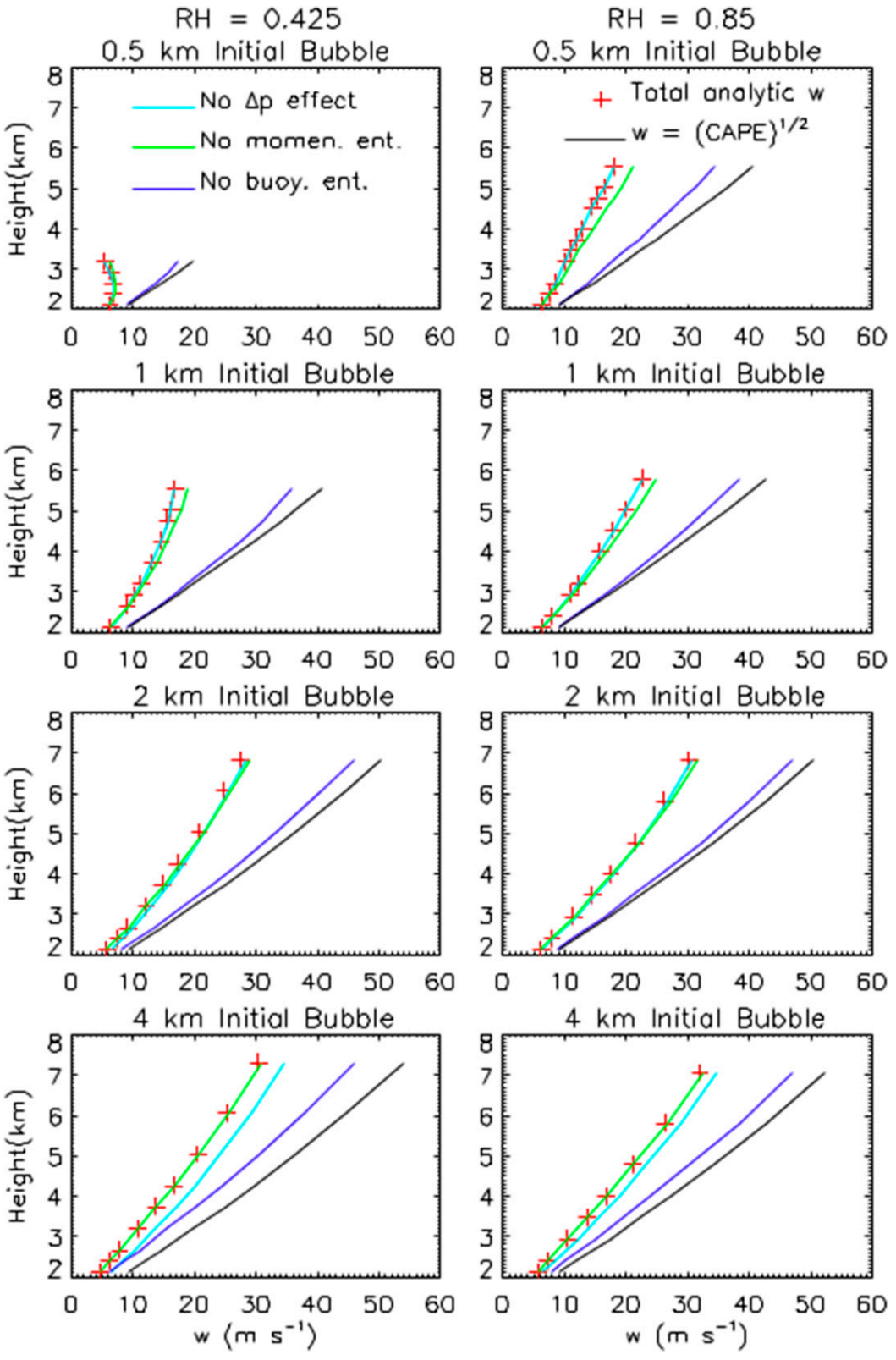

FIG. 12. Vertical velocity w at the updraft center and height of maximum buoyancy as it rises over time, from the analytic solutions calculated using (26). The total analytic w with all processes included is indicated by red plus signs, and colored lines indicate solutions neglecting either B entrainment (purple) or w entrainment (green). Individual data points are plotted at 1-min intervals. The thermodynamic maximum w is shown by the solid black line.

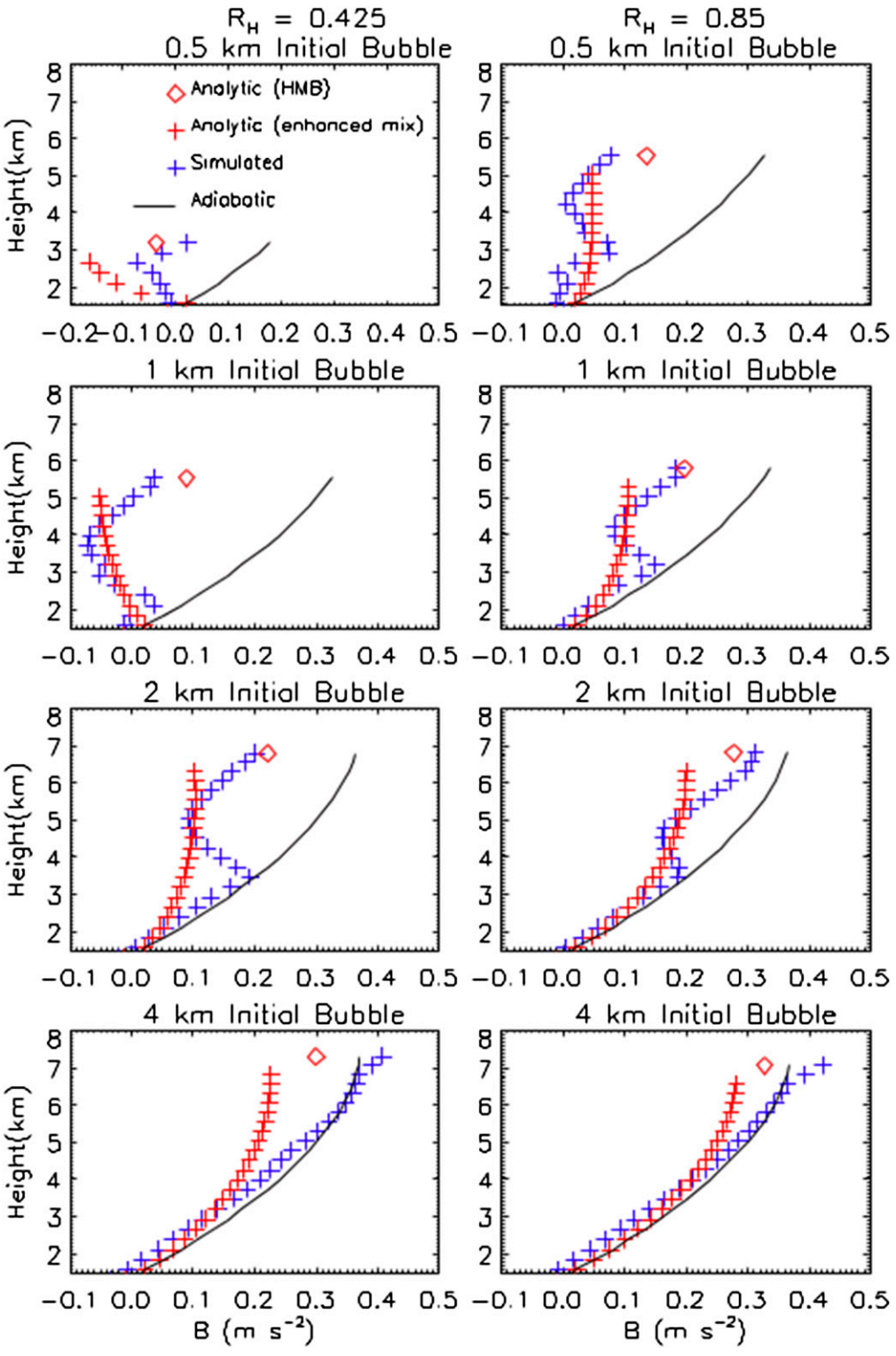

FIG. 13. Vertical profiles of buoyancy at the updraft center from the simulations (blue crosses), the analytic expression at the HMB from (23) (red diamonds), and the analytic expression between the LFC and HMB with enhanced lateral mixing from (32) (red crosses). The pseudoadiabatic buoyancy is shown by the solid black line. Profiles are shown at the time when the HMB achieves maximum height (up to 7.5 km) in each simulation. Note that the profiles of buoyancy are only shown up to the HMB, since this region is where the analytic expressions are valid.

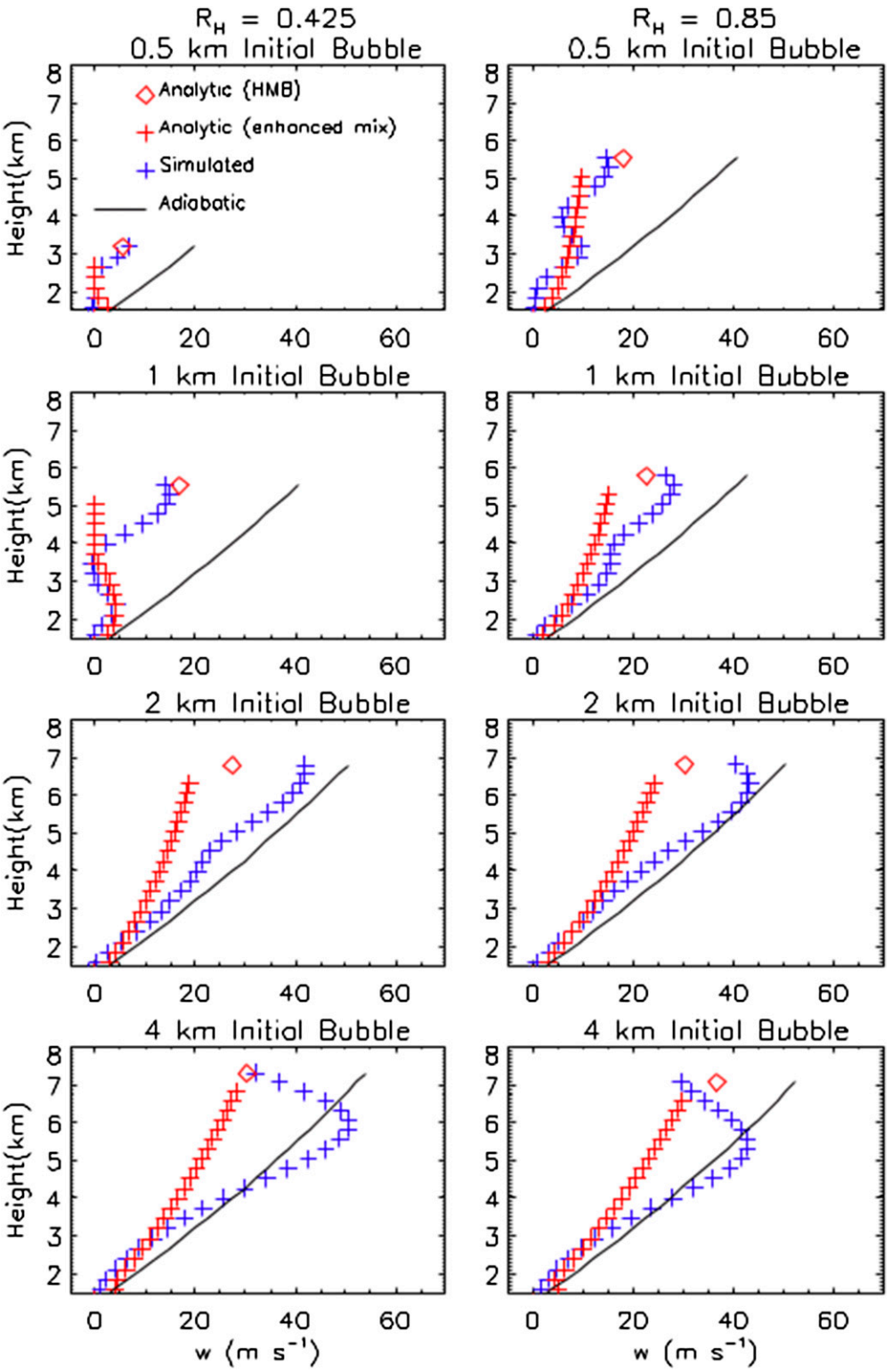

FIG. 14. As in Fig. 13, but for vertical velocity w. Results are shown for the analytic expression at the HMB given by (26) (red diamonds) and between the LFC and HMB with enhanced lateral mixing following (33) (red crosses). The thermodynamic maximum w is shown by the solid black line. Note that the profiles of w are only shown up to the HMB, since this region is where the analytic expressions are valid.

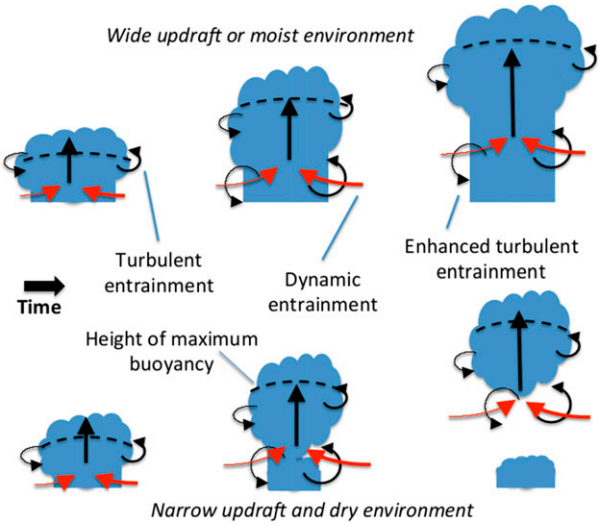

FIG. 15. Conceptual model of growing deep moist convective updrafts. Features illustrated are lateral turbulent entrainment (small curved black arrows) near the HMB as it rises over time (dashed line), dynamic entrainment associated with lateral inflow of environmental air (red arrows), and enhanced lateral turbulent mixing (large curved black arrows) below the HMB due to sharpening of horizontal gradients from dynamic entrainment. The blue shaded region represents the updraft region with positive buoyancy and vertical velocity. The upper (lower) sequence represents a wide (narrow) updraft in a moist (dry) environment.

and the updrafts exhibit little dilution, even for narrow updrafts. When L is also set to 100 m in the analytic expressions, they give similar results as the corresponding numerical simulations except with somewhat greater dilution. This small difference likely occurs because horizontal gradients near the lateral updraft edge are sharper with the reduced mixing in the simulations, differing from the linear horizontal gradients assumed in the analytic derivations.

To analyze mixing in detail, a passive tracer with a mixing ratio of 1 kg kg^{-1} was added in the model, with values of the tracer held fixed below the eighth model vertical layer above the surface (approximately 1800 m, just above the LFC).

b. *Overview of numerical simulation results*

Updraft evolution in the simulations is illustrated by vertical cross sections of perturbation potential temperature θ', vertical air velocity w, and horizontal air velocity u at various times (Figs. 4–7). Results from the 1- and 4-km initial bubble simulations with $R_H = 0.425$ and $R_H = 0.85$ are shown. A few common features are evident in all of the simulations. Rapid updraft growth ensues once condensation begins. After the updrafts grow sufficiently deep, there is a sharp narrowing of the updraft radius R (defined by the region with $B > 0$ and $w > 0$) just below the HMB, located about 1 km below the rising cloud top. This narrowing is associated with dynamic entrainment as discussed in section 2d. After about 15–20 min the buoyancy at the HMB begins to decrease as a result of entrainment and dilution, and eventually a new HMB is established lower in the updraft. Updraft radius at the HMB is fairly steady in time as the updrafts grow, especially for the drier environment (Fig. 8).

While these simulations share some common features, there are notable differences. Updraft radius and environmental R_H have a strong impact on convective evolution, as anticipated from the theoretical expressions. The 1-km initial bubble and $R_H = 0.425$ simulation (Fig. 4) exhibits much greater dilution than the others shown in Figs. 5–7, with a rapid reduction of buoyancy over time and a deep negatively buoyant region between the LFC and the HMB consistent with the theoretical expressions and discussion in section 2d. That is, the buoyant updraft becomes detached from the LFC as it grows, exhibiting the structure of a rising thermal instead of a plume. In contrast, the simulation with a 1-km initial bubble but moist environment ($R_H = 0.85$) and both the moist and dry simulations with 4-km initial bubbles have a continuous region of positive buoyancy below the HMB that is clearly rooted at the LFC and, hence, have a structure more consistent with plumes.

4. Comparison of the theoretical expressions and numerical simulations

This section compares the theoretical expressions for evolution of C_{Tr}, B, and w at the updraft center in section 2 with the numerical simulations described in section 3. Results are first compared at the HMB as it rises over time in the simulations using the analytic expressions for C_{Tr}, B, and w given by (11), (23), and (26), respectively. Then, profiles of B and w between the LFC and HMB from the simulations and analytic expressions from (32) and (33) are compared.

a. *Scalar at the HMB*

The analytic [(11)] and simulated ratios $C_{\mathrm{Tr},z}/C_{\mathrm{Tr},0}$ as a function of z (time) at the updraft center ($r = 0$) for the four different initial bubble radii (0.5, 1, 2, and 4 km) are compared in Fig. 9. Simulations using $R_H = 0.425$ are presented (results are similar for the $R_H = 0.85$ simulations, not shown). Following the discussion in section 2a, R, z, and $C_{\mathrm{Tr},z}/C_{\mathrm{Tr},0}$ are taken at the HMB (up to 7.5 km, the approximate height of maximum buoyancy of the sounding assuming pseudoadiabatic ascent). Here, R is defined by the width of the region with $C_{\mathrm{Tr}} > 0.01$ in each simulation, averaged over height (time)

from the LFC to z. This definition of R is somewhat arbitrary, but results do not depend much on the particular threshold chosen for C_{Tr} less than 0.1. The same threshold is applied for all cases analyzed here. Values of $k^2/P_r = 0.2$ and $L = 500$ m are used in (11) for the analytic solutions consistent with the mixing parameters used in WRF.

The analytic solutions are reasonably similar to the numerically simulated $C_{\mathrm{Tr},z}/C_{\mathrm{Tr},0}$. There is generally greater dilution (smaller $C_{\mathrm{Tr},z}/C_{\mathrm{Tr},0}$) with an increase in z, except for the 4-km initial bubble simulation updraft, which remains nearly undiluted. Dilution increases with z at a faster rate for narrower updrafts than wider ones, illustrating the inverse dependence on R. The main difference is somewhat less dilution, especially at midlevels (~4–7-km height), for the 2- and 4-km bubble simulations compared to the analytic solutions. This appears to be caused by the fact that horizontal gradients of w and C_{Tr} near the updraft center at the HMB are small early in these simulations, while the analytic solutions assume that $\partial w/\partial r \approx -w/R$ and $\partial C/\partial r \sim -(C_{\mathrm{Tr}} - C_{\mathrm{Tr},E})/R$, which provides a better approximation of the horizontal gradients during later updraft growth.

b. Buoyancy at the HMB

The analytic B at the updraft center from (23) is compared to that from the simulations in Fig. 10. The pseudoadiabatic buoyancy B_{AD} is calculated directly from the initial sounding based on pseudoadiabatic ascent of the most energetic parcel. Since the initial warm bubble extends above the LFC and values of B just above the LFC are strongly influenced by the initial conditions of the bubble, the z in (23) is taken as the height above 2000 m, ~500 m above the LFC (this height was chosen because values of B below it tend to be superadiabatic in the simulations). The value of R is calculated from the simulations by the width of the region with $B > 0$ and $w > 0$ at the HMB and is averaged over the time for parcels to travel from the LFC to z. As noted earlier, for simplicity the analytic expressions for B and w neglect the occurrence of a moist descending shell around the lateral updraft edge, and assume entrained air has the same properties as the environment. Values of $k^2/P_r = 0.2$ and $L = 500$ m are used for the analytic solutions for consistency with the simulations, similar to the comparison of C_{Tr}.

The analytic solutions well capture the simulated B, including its decrease with height relative to B_{AD} due to dilution, its decrease with initial bubble width, and its decrease with environmental R_H. The effects of lower R_H are most apparent when R is small, while the effects are much less apparent for wider updrafts. Notably, the analytic solution captures the rapid decrease of B to negative values at a height above ~3 km for the narrowest updraft (0.5-km initial bubble) and dry environment ($R_H = 0.425$), broadly consistent with LES showing that the cloud field remains shallow in dry environments even when there is appreciable CAPE (Derbyshire et al. 2004). The analytic and numerical results showing larger updrafts are less diluted above cloud base than their narrower counterparts are also consistent with previous LES studies (e.g., Kuang and Bretherton 2006; Khairoutdinov and Randall 2006).

c. Vertical velocity at the HMB

Figure 11 compares the analytic w at the updraft center calculated using (26) with that from the simulations. The value of R is calculated in the same manner as it was for buoyancy in section 4b, the same k^2 as applied to C_{Tr} and B is used in (26) for consistency, and α is calculated directly from the simulations. The variable H is the distance between the HMB and the LFC. Overall, the analytic and numerical solutions are similar, and both indicate much smaller w compared to w_{max}. Note that w is small compared to w_{max} near the LFC for the 4-km initial bubble simulations, despite almost no dilution by entrainment. This behavior is captured by the analytic solutions, and results from a strong downward-directed perturbation pressure gradient force. The analytic solutions reproduce the smaller increase of w (or even decrease) with height for narrower updrafts from the simulations due to lateral mixing, especially in the drier environment. For $R_H = 0.425$ and the narrowest updraft, both the analytic and numerical solutions show a decrease of w with height.

The contrasting effects of entrainment and perturbation pressure are further illustrated in Fig. 12, which shows the analytic w from (26) following the HMB as it rises over time for the simulated cases, but with various entrainment terms neglected (no w momentum entrainment or no B entrainment). The entrainment of B (including entrainment of dry air) is important in all cases at heights of ~1 km or more above LFC, particularly for narrower updrafts in the drier environment. The effects of w momentum entrainment are small, with less than ~15% change in w when neglected in all cases and almost no effect for the 2- and 4-km initial bubbles. The limited impact of momentum entrainment on acceleration is consistent with LES (Dawe and Austin 2011b; de Roode et al. 2012; Sherwood et al. 2013). Perturbation pressure effects are negligible for the narrower updrafts (initial bubble radii of 0.5 and 1 km) because of the small updraft aspect ratios (R/H) but are important for the 4-km initial bubble cases near the LFC when H is small and hence R/H is relatively large. This is

shown in Fig. 12 by the difference between the no B entrainment calculation (purple lines) and the thermodynamic maximum w (black lines); since w entrainment is minimal, this difference is due to perturbation pressure effects.

d. *Buoyancy and vertical velocity between the LFC and HMB*

We next compare the theoretical expressions and simulations between the LFC and HMB, where dynamic entrainment plays an important role by enhancing lateral turbulent mixing compared to that at the HMB as discussed in section 2d. Profiles of simulated B and w between the LFC and HMB and those from the analytic expressions given (32) and (33), respectively, are compared at the time when the HMB is at its maximum height (up to 7.5 km) in Fig. 13 (a comparison at earlier times is similar). Overall, the analytic expressions and simulations give similar profiles of B. In particular, both the analytic expressions and numerical solutions produce a deep region of negative B between the LFC and HMB for the dry cases with 0.5- and 1-km initial bubbles. This supports the idea that dynamic entrainment leads to thermal-like structure when updrafts are narrow, relative to z, and the environment is dry, as opposed to plume-like structure when updrafts are wider or the environment is moister. Interestingly, the linkage between dynamic entrainment and vertical acceleration might also explain the rising pulse-like features seen in the simulations (the local peaks of B and w at midlevels in some of the simulations, cf. Fig. 5, and also seen in the profiles in Fig. 13). That is, the negative feedback between dynamic entrainment and $\partial w/\partial z$ (i.e., an increase in $\partial w/\partial z$ leads to greater dynamic entrainment, thereby reducing $\partial w/\partial z$) may lead to a pulse-like updraft evolution, similar to the mechanism proposed by Heus et al. (2009). The analytic model cannot capture this behavior because it assumes linear profiles of quantities above the LFC.

The analytic expression for w between the LFC and HMB from (33) gives results similar to the simulations for the 0.5- and 1-km initial bubble cases, but it does not work as well for the 2- and 4-km initial bubble cases (Fig. 14). This is likely due to the role of local vertical dynamic perturbation pressure gradients on w that are not included in the analytic expressions. The effects of dynamic perturbation pressure are greatest for the wider updrafts since they have the largest w and hence the largest magnitude of $\partial w/\partial z$. While vertical gradients of dynamic perturbation pressure can be important locally (Peters 2016), especially in driving vertical acceleration lower in the updraft, the impact on overall vertical acceleration averaged from the updraft bottom to top is generally small (Morrison 2016a; Peters 2016).

5. Discussion and conclusions

This paper presented new analytic expressions for the evolution of a passive scalar C_{Tr}, buoyancy B, and vertical velocity w in growing, entraining deep moist convective updrafts. These expressions gave C_{Tr}, B, and w as a function of R, z, environmental R_H, and CAPE, similar to 3D numerical simulations in which convection was initiated by warm bubbles of varying size in either a dry or a moist environment. In particular, the analytic expressions captured the mixing out of narrow buoyant updrafts a few kilometers above the LFC in low-R_H environments despite the occurrence of large CAPE. These expressions also theoretically describe the opposing dependencies of perturbation pressure and entrainment effects as they vary with R, such that entrainment reduces w of narrow updrafts more than that of wide ones, while perturbation pressure effects weaken wide updrafts more than narrow ones. This results in a maximum w occurring at intermediate updraft sizes with R of approximately 1–5 km, depending upon the mixing coefficients and height above the level of free convection (LFC).

Results suggested different scalings for the lateral entrainment rate near the height of maximum buoyancy (HMB), located about 1 km below the updraft top, and lower in the updraft between the LFC and the HMB owing to the effects of dynamic entrainment, which contrasts with the standard entraining-plume model. Near the HMB, dynamic entrainment is limited because net horizontal convergence across the updraft there is small, dictated primarily by the vertical distribution of buoyancy within the updraft. Between the LFC and HMB, dynamic entrainment associated with inflow of environmental air leads to a sharpening of horizontal gradients and hence enhanced lateral turbulent mixing. Thus, the effects of organized updraft-scale flow and smaller-scale turbulent mixing through entrainment are inextricably linked, consistent with the idea of kinetic energy and scalar variance cascades from larger-scale eddies to the smaller-scale eddies that ultimately drive mixing.

Results showed an enhancement of lateral turbulent mixing between the LFC and HMB relative to the HMB by a factor of ~9/4 independent of R, z, or w, suggesting self-similarity of dynamic entrainment and its effects on mixing and dilution. For narrow updrafts (relative to height) in a dry environment, this enhanced turbulent mixing led to the ascending region of positive buoyancy near the HMB being "cut off" from the LFC by a region

of negative buoyancy, in essence leading to a rising-thermal-like structure rather than a plume-like updraft structure. This effect was captured by the theoretical expressions and evident in the simulations. Thus, it is proposed that dynamic entrainment, leading to enhanced lateral turbulent mixing between the LFC and HMB, provides a bridge between the plume and thermal conceptual models, with the transition between a plume-like structure and a thermal-like structure dictated by updraft width relative to height and environmental R_H. These results are summarized in a simple conceptual model of an isolated, growing moist deep convective updraft (Fig. 15). Further testing is needed using LES to confirm this finding for less-idealized conditions.

As in any study, there are several caveats that should be kept in mind. The most important is that the numerical simulations were highly idealized by representing updrafts as diffusive moist bubbles and did not resolve a spectrum of eddies expected to occur in turbulent updrafts. Larger eddies associated with organized convective-scale flow were well resolved in all of the simulations, while smaller-scale turbulent mixing was parameterized by a first-order subgrid-scale closure with a fixed mixing length. This idealized approach was taken in order to control the updraft size at the stage of initiation, to allow a direct comparison with the theoretical expressions, and to simplify the analysis and interpretation by virtue of horizontal symmetry around the updraft center. Thus, the simulations were not LES. The impact of resolving turbulent eddies in assessing the theoretical expressions is unknown but potentially important and should be investigated in future work.

It was also assumed that the environment was initially unsheared for simplicity; it is expected that adding shear could have important impacts on entrainment by affecting the mixing coefficients, among others. Finally, the effects of condensate loading on updraft buoyancy were neglected. Since condensation rate was included in the theoretical derivation, it should be possible to combine the expression for buoyancy with a conservation equation for cloud mass mixing ratio.

Acknowledgments. This work was partially supported by U.S. DOE ASR DE-SC0008648, NASA NNX14AO85G, and the NSF Science and Technology Center for Multiscale Modeling of Atmospheric Processes (CMMAP), managed by Colorado State University under Cooperative Agreement ATM-0425247. Comments on an earlier version of the manuscript by R. Rotunno, W. Grabowski, and V. Larson are appreciated. Comments on the manuscript by J. Peters and two anonymous reviewers are also appreciated and helped to improve the manuscript. High-performance computing support on Yellowstone was provided by NCAR's Computational and Information Laboratory, sponsored by the NSF.

REFERENCES

Asai, T., and A. Kasahara, 1967: A theoretical study of compensating downward motions associated with cumulus clouds. *J. Atmos. Sci.*, **24**, 487–496, doi:10.1175/1520-0469(1967)024<0487:ATSOTC>2.0.CO;2.

Batchelor, G. K., 1954: Heat convection and buoyancy effects in fluids. *Quart. J. Roy. Meteor. Soc.*, **80**, 339–358, doi:10.1002/qj.49708034504.

Bechtold, P., M. Kohler, T. Jung, F. Doblas-Reyes, M. Leutbecher, M. Rodwell, F. Vitart, and G. Balsamo, 2008: Advances in simulating atmospheric variability with the ECMWF model: From synoptic to decadal time-scales. *Quart. J. Roy. Meteor. Soc.*, **134**, 1337–1351, doi:10.1002/qj.289.

Betts, A. K., 1975: Parametric interpretation of trade-wind cumulus budget studies. *J. Atmos. Sci.*, **32**, 1934–1945, doi:10.1175/1520-0469(1975)032<1934:PIOTWC>2.0.CO;2.

Boing, S. J., H. J. J. Jonker, W. A. Narawa, and A. P. Siebesma, 2014: On the deceiving aspects of mixing diagrams of deep cumulus convection. *J. Atmos. Sci.*, **71**, 56–68, doi:10.1175/JAS-D-13-0127.1.

Bretherton, C. S., J. R. McCaa, and H. Grenier, 2004: A new parameterization for shallow cumulus convection and its application to marine subtropical cloud-topped boundary layers. Part I: Description of 1D results. *Mon. Wea. Rev.*, **132**, 864–882, doi:10.1175/1520-0493(2004)132<0864:ANPFSC>2.0.CO;2.

Chow, F. K., R. L. Street, M. Xue, and J. H. Feriger, 2005: Explicit filtering and reconstruction turbulence modeling for large-eddy simulation of neutral boundary layer flow. *J. Atmos. Sci.*, **62**, 2058–2077, doi:10.1175/JAS3456.1.

Dawe, J. T., and P. H. Austin, 2011a: Interpolation of LES cloud surface for use in direct calculations of entrainment and detrainment. *Mon. Wea. Rev.*, **139**, 444–456, doi:10.1175/2010MWR3473.1.

——, and ——, 2011b: The influence of the cloud shell on tracer budget measurements of LES cloud entrainment. *J. Atmos. Sci.*, **68**, 2909–2920, doi:10.1175/2011JAS3658.1.

Deardorff, J. W., 1972: Numerical investigation of neutral and unstable planetary boundary layers. *J. Atmos. Sci.*, **29**, 91–115, doi:10.1175/1520-0469(1972)029<0091:NIONAU>2.0.CO;2.

Derbyshire, S. H., I. Beau, P. Bechtold, J.-Y. Grandpeix, J.-M. Piriou, J.-L. Rdelsperger, and P. M. M. Soares, 2004: Sensitivity of moist convection to environmental humidity. *Quart. J. Roy. Meteor. Soc.*, **130**, 3055–3079, doi:10.1256/qj.03.130.

de Roode, S. R., A. P. Siebesma, H. J. J. Jonker, and Y. de Voogd, 2012: Parameterization of the vertical velocity equation for shallow convection. *Mon. Wea. Rev.*, **140**, 2424–2436, doi:10.1175/MWR-D-11-00277.1.

de Rooy, W. C., and A. P. Siebesma, 2010: Analytic expressions for entrainment and detrainment in cumulus convection. *Quart. J. Roy. Meteor. Soc.*, **136**, 1216–1227, doi:10.1002/qj.640.

——, P. Bechtold, K. Frolich, C. Hohenegger, H. Jonker, D. Mironov, A. P. Siebesma, J. Teixeira, and J.-I. Yano, 2013: Entrainment and detrainment in cumulus convection: An overview. *Quart. J. Roy. Meteor. Soc.*, **139**, 1–19, doi:10.1002/qj.1959.

Emanuel, K. A., 1991: A scheme for representing cumulus convection in large-scale models. *J. Atmos. Sci.*, **48**, 2313–2335, doi:10.1175/1520-0469(1991)048<2313:ASFRCC>2.0.CO;2.

——, 1994: *Atmospheric Convection.* Oxford University Press, 580 pp.

Grabowski, W. W., and T. L. Clark, 1993: Cloud-environment interface instability. Part II: Extension to three spatial dimensions. *J. Atmos. Sci.*, **50**, 555–573, doi:10.1175/1520-0469(1993)050<0555:CEIIPI>2.0.CO;2.

Heus, T., and H. J. J. Jonker, 2008: Subsiding shells around shallow cumulus clouds. *J. Atmos. Sci.*, **65**, 1003–1018, doi:10.1175/2007JAS2322.1.

——, G. Van Dijk, H. J. J. Jonker, and H. E. A. Van den Akker, 2008: Mixing in shallow cumulus clouds studied by Lagrangian particle tracking. *J. Atmos. Sci.*, **65**, 2581–2597, doi:10.1175/2008JAS2572.1.

——, H. J. J. Jonker, H. E. A. van den Akker, E. J. Griffith, M. Loutek, and F. H. Post., 2009: A statistical approach to the lifecycle analysis of cumulus clouds selected in a virtual reality environment. *J. Geophys. Res.*, **114**, D06208, doi:10.1029/2008JD010917.

Holton, J. R., 1973: A one-dimensional cumulus model including pressure perturbations. *Mon. Wea. Rev.*, **101**, 201–205, doi:10.1175/1520-0493(1973)101<0201:AOCMIP>2.3.CO;2.

Houghton, H. G., and H. E. Cramer, 1951: A theory of entrainment in convective currents. *J. Meteor.*, **8**, 95–102, doi:10.1175/1520-0469(1951)008<0095:ATOEIC>2.0.CO;2.

Jonas, P. R., 1990: Observations of cumulus cloud entrainment. *Atmos. Res.*, **25**, 105–127, doi:10.1016/0169-8095(90)90008-Z.

Jonker, H. J. J., T. Heus, and P. P. Sullivan, 2008: A refined review of vertical mass transport by cumulus convection. *J. Geophys. Res.*, **35**, L07810, doi:10.1029/2007GL032606.

Kain, J. S., and J. M. Fritsch, 1990: A one-dimensional entraining/detraining plume model and its application in convective parameterization. *J. Atmos. Sci.*, **47**, 2784–2802, doi:10.1175/1520-0469(1990)047<2784:AODEPM>2.0.CO;2.

Khairoutdinov, M., and D. Randall, 2006: High-resolution simulation of shallow to deep convection transition over land. *J. Atmos. Sci.*, **63**, 3421–3436, doi:10.1175/JAS3810.1.

Kuang, Z., and C. S. Bretherton, 2006: A mass-flux scheme view of a high-resolution simulation of a transition from shallow to deep cumulus convection. *J. Atmos. Sci.*, **63**, 1895–1909, doi:10.1175/JAS3723.1.

Kuo, H. L., 1962: On the controlling influences of eddy diffusion on thermal convection. *J. Atmos. Sci.*, **19**, 236–243, doi:10.1175/1520-0469(1962)019<0236:OTCIOE>2.0.CO;2.

——, and W. H. Raymond, 1980: A quasi-one-dimensional cumulus cloud model and parameterization of cumulus heating and mixing effects. *Mon. Wea. Rev.*, **108**, 991–1009, doi:10.1175/1520-0493(1980)108<0991:AQODCC>2.0.CO;2.

Lebo, Z. J., and H. Morrison, 2015: Effects of horizontal and vertical grid spacing on mixing in simulated squall lines and implications for convective strength and structure. *Mon. Wea. Rev.*, **143**, 4355–4375, doi:10.1175/MWR-D-15-0154.1.

Moeng, C.-H., M. A. LeMone, M. F. Khairoutdinov, S. K. Krueger, P. A. Bogenschutz, and D. A. Randall, 2009: The tropical marine boundary layer under a deep convection system: A large-eddy simulation study. *J. Adv. Model. Earth Syst.*, **1** (16), doi:10.3894/JAMES.2009.1.16.

Morrison, H., 2016a: Impacts of updraft size and dimensionality on the perturbation pressure and vertical velocity in cumulus convection. Part I: Simple, generalized analytic solutions. *J. Atmos. Sci.*, **73**, 1441–1454, doi:10.1175/JAS-D-15-0040.1.

——, 2016b: Impacts of updraft size and dimensionality on the perturbation pressure and vertical velocity in cumulus convection. Part II: Comparison of theoretical and numerical solutions and dully dynamical simulations. *J. Atmos. Sci.*, **73**, 1455–1480, doi:10.1175/JAS-D-15-0041.1.

——, G. Thompson, and V. Tatarskii, 2009: Impact of cloud microphysics on the development of trailing stratiform precipitation in a simulated squall line: Comparison of one- and two-moment schemes. *Mon. Wea. Rev.*, **137**, 991–1007, doi:10.1175/2008MWR2556.1.

Morton, B. R., G. Taylor, and J. S. Turner, 1956: Turbulent gravitational convection from maintained and instantaneous sources. *Proc. Roy. Soc. London*, **234A**, 1–23, doi:10.1098/rspa.1956.0011.

Neggers, R. A. J., A. P. Siebesma, and H. J. J. Jonker, 2002: A multiparcel method for shallow cumulus convection. *J. Atmos. Sci.*, **59**, 1655–1668, doi:10.1175/1520-0469(2002)059<1655:AMMFSC>2.0.CO;2.

Paluch, I. R., 1979: The entrainment of air in Colorado cumuli. *J. Atmos. Sci.*, **36**, 2467–2478, doi:10.1175/1520-0469(1979)036<2467:TEMICC>2.0.CO;2.

Peters, J. M., 2016: The impact of relative buoyancy and dynamic pressure forcing on vertical velocities within two-dimensional updrafts. *J. Atmos. Sci.*, **73**, 4531–4551, doi:10.1175/JAS-D-16-0016.1.

Raymond, D. J., and A. M. Blyth, 1986: A stochastic mixing model for nonprecipitating cumulus clouds. *J. Atmos. Sci.*, **43**, 2708–2718, doi:10.1175/1520-0469(1986)043<2708:ASMMFN>2.0.CO;2.

Romps, D. M., 2010: A direct measure of entrainment. *J. Atmos. Sci.*, **67**, 1908–1927, doi:10.1175/2010JAS3371.1.

——, 2016: The stochastic parcel model: A deterministic parameterization of stochastically entraining convection. *J. Adv. Model. Earth Syst.*, **8**, 319–344, doi:10.1002/2015MS000537.

——, and Z. M. Kuang, 2010: Do undiluted convective plumes exist in the upper tropical troposphere? *J. Atmos. Sci.*, **67**, 468–484, doi:10.1175/2009JAS3184.1.

Sherwood, S. C., D. Hernandez-Deckers, M. Colin, and F. Robinson, 2013: Slippery thermals and cumulus entrainment paradox. *J. Atmos. Sci.*, **70**, 2426–2442, doi:10.1175/JAS-D-12-0220.1.

Siebesma, A. P., 1998: Shallow cumulus convection. *Buoyant Convection in Geophysical Flows*, E. J. Pate et al., Eds., Kluwer Academic Publishers, 441–486.

——, and J. W. M. Cuijpers, 1995: Evaluation of parametric assumptions for shallow cumulus convection. *J. Atmos. Sci.*, **52**, 650–666, doi:10.1175/1520-0469(1995)052<0650:EOPAFS>2.0.CO;2.

——, and Coauthors, 2003: A large eddy simulation intercomparison study of shallow cumulus convection. *J. Atmos. Sci.*, **60**, 1201–1219, doi:10.1175/1520-0469(2003)60<1201:ALESIS>2.0.CO;2.

Skamarock, W. C., 2004: Evaluating mesoscale NWP models using kinetic energy spectra. *Mon. Wea. Rev.*, **132**, 3019–3032, doi:10.1175/MWR2830.1.

——, and Coauthors, 2008: A description of the Advanced Research WRF version 3. NCAR Tech. Note NCAR/TN-475+STR, 113 pp., doi:10.5065/D68S4MVH.

Smagorinsky, J., 1963: General circulation experiments with the primitive equations. I. The basic experiment. *Mon. Wea. Rev.*, **91**, 99–164, doi:10.1175/1520-0493(1963)091<0099:GCEWTP>2.3.CO;2.

Squires, P., and J. S. Turner, 1962: An entraining jet model for cumulo-nimbus updrafts. *Tellus*, **14A**, 422–434, doi:10.3402/tellusa.v14i4.9569.

Taylor, B. R., and M. B. Baker, 1991: Entrainment and detrainment in cumulus clouds. *J. Atmos. Sci.*, **48**, 112–121, doi:10.1175/1520-0469(1991)048<0112:EADICC>2.0.CO;2.

Tiedtke, M., 1989: A comprehensive mass flux scheme for cumulus parameterization in large-scale models. *Mon. Wea. Rev.*, **117**, 1779–1800, doi:10.1175/1520-0493(1989)117<1779:ACMFSF>2.0.CO;2.

Turner, J. S., 1962: The starting plume in neutral surroundings. *J. Fluid Mech.*, **13**, 356–368, doi:10.1017/S0022112062000762.

——, 1973: *Buoyancy Effects in Fluids.* Cambridge University Press, 368 pp.

Warner, J., 1970: On steady-state one-dimensional models of cumulus convection. *J. Atmos. Sci.*, **27**, 1035–1040, doi:10.1175/1520-0469(1970)027<1035:OSSODM>2.0.CO;2.

——, 1977: Time variation of updraft and water content in small cumulus clouds. *J. Atmos. Sci.*, **34**, 1306–1312, doi:10.1175/1520-0469(1977)034<1306:TVOUAW>2.0.CO;2.

Weisman, M. L., and J. B. Klemp, 1982: The dependence of numerically simulated convective storms on vertical wind shear and buoyancy. *Mon. Wea. Rev.*, **110**, 504–520, doi:10.1175/1520-0493(1982)110<0504:TDONSC>2.0.CO;2.